# Ly$\alpha$ emitters with very large Ly$\alpha$ equivalent widths, EW0(Ly$\alpha$) 200-400 Å, at z $\sim$ 2

Takuya Hashimoto, Masami Ouchi, Kazuhiro Shimasaku, Daniel Schaerer, Kimihiko Nakajima, Takatoshi Shibuya, Yoshiaki Ono, Michael Rauch, Ryosuke Goto

Monthly Notices
of the
ROYAL ASTRONOMICAL SOCIETY

MNRAS **465,** 1543–1562 (2017)
Advance Access publication 2016 November 4

doi:10.1093/mnras/stw2834

# Lyα emitters with very large Lyα equivalent widths, $EW_0$(Lyα) ≃ 200–400 Å, at $z \sim 2$

Takuya Hashimoto,[1,2★] Masami Ouchi,[3,4] Kazuhiro Shimasaku,[1,5] Daniel Schaerer,[6] Kimihiko Nakajima,[6,7] Takatoshi Shibuya,[3] Yoshiaki Ono,[3] Michael Rauch[8] and Ryosuke Goto[1,9]

[1]*Department of Astronomy, Graduate School of Science, The University of Tokyo, Tokyo 113-0033, Japan*
[2]*Centre de Recherche Astrophysique de Lyon, Université de Lyon, Université Lyon 1, Observatoire de Lyon, Ecole Normale Supérieure de Lyon, CNRS, UMR 5574, 9 avenue Charles André, Saint Genis Laval F-69230, France*
[3]*Institute for Cosmic Ray Research, The University of Tokyo, 5-1-5 Kashiwanoha, Kashiwa, Chiba 277-8582, Japan*
[4]*Kavli Institute for the Physics and Mathematics of the Universe (WPI), The University of Tokyo, 5-1-5 Kashiwanoha, Kashiwa, Chiba 277-8583, Japan*
[5]*Research Center for the Early Universe, Graduate School of Science, The University of Tokyo, Tokyo 113-0033, Japan*
[6]*Observatoire de Genève, Université de Genève, 51 Ch. des Maillettes, CH-1290 Versoix, Switzerland*
[7]*European Southern Observatory, Karl-Schwarzschild-Straße 2, D-85748 Garching, Germany*
[8]*Observatories of the Carnegie Institution of Washington, 813 Santa Barbara Street, Pasadena, CA 91101, USA*
[9]*VASILY, Inc. 2-23-5 Nishigotanda, Shinagawa-ku, Tokyo, 141-0031, Japan*

Accepted 2016 November 1. Received 2016 November 1; in original form 2016 September 6

## ABSTRACT

We present physical properties of spectroscopically confirmed Lyα emitters (LAEs) with very large rest-frame Lyα equivalent widths $EW_0$(Lyα). Although the definition of large $EW_0$(Lyα) LAEs is usually difficult due to limited statistical and systematic uncertainties, we identify six LAEs selected from ∼3000 LAEs at $z \sim 2$ with reliable measurements of $EW_0$ (Lyα) ≃ 200–400 Å given by careful continuum determinations with our deep photometric and spectroscopic data. These large $EW_0$(Lyα) LAEs do not have signatures of AGN, but notably small stellar masses of $M_\star = 10^{7-8}\,M_\odot$ and high specific star formation rates (star formation rate per unit galaxy stellar mass) of ∼100 $Gyr^{-1}$. These LAEs are characterized by the median values of $L(\text{Ly}\alpha) = 3.7 \times 10^{42}$ erg $s^{-1}$ and $M_{UV} = -18.0$ as well as the blue UV continuum slope of $\beta = -2.5 \pm 0.2$ and the low dust extinction $E(B-V)_* = 0.02^{+0.04}_{-0.02}$, which indicate a high median Lyα escape fraction of $f_{esc}^{Ly\alpha} = 0.68 \pm 0.30$. This large $f_{esc}^{Ly\alpha}$ value is explained by the low H I column density in the interstellar medium which is consistent with full width at half-maximum (FWHM) of the Lyα line, FWHM(Lyα) = 212 ± 32 km $s^{-1}$, significantly narrower than those of small $EW_0$(Lyα) LAEs. Based on the stellar evolution models, our observational constraints of the large $EW_0$ (Lyα), the small $\beta$, and the rest-frame He II EW imply that at least a half of our large $EW_0$(Lyα) LAEs would have young stellar ages of ≲20 Myr and very low metallicities of $Z < 0.02\,Z_\odot$ regardless of the star formation history.

**Key words:** galaxies: evolution – galaxies: formation – galaxies: high-redshift – cosmology: observations.

## 1 INTRODUCTION

Photometric studies of Lyα emitters (LAEs; Cowie & Hu 1998; Rhoads et al. 2000; Ouchi et al. 2003; Malhotra & Rhoads 2004; Gronwall et al. 2007) have revealed that about 4–10 per cent (10–40 per cent) of LAEs at $z \sim 2$–3 ($z \sim 4$–6) show extremely large rest-frame Lyα equivalent widths, $EW_0$ (Lyα) ≳ 200 Å ($z \sim 2$–3, Nilsson et al. 2007; Mawatari et al. 2012; $z \sim 4$–6, Malhotra & Rhoads 2002; Shimasaku et al. 2006; Ouchi et al. 2008; Zheng et al. 2014). Several spectroscopic studies have also identified LAEs with large $EW_0$ (Lyα) values (Dawson et al. 2004; Wang et al. 2009; Adams et al. 2011; Kashikawa et al. 2012).

Schaerer (2003) and Raiter, Schaerer & Fosbury (2010) have constructed stellar evolution models which cover various metallicities ($Z = 0$–$1.0\,Z_\odot$) and a wide range of initial mass functions (IMFs). According to the models of Schaerer (2003) and Raiter et al. (2010), the value of $EW_0$ (Lyα) ≳ 200 Å can be explained

★ E-mail: thashimoto@astron.s.u-tokyo.ac.jp

by stellar populations with a very young stellar age ($\lesssim$10 Myr), a very low metallicity, or a top-heavy IMF (cf. Charlot & Fall 1993; Malhotra & Rhoads 2002). Thus, large EW$_0$(Ly$\alpha$) LAEs are particularly interesting as candidates for galaxies at an early stage of the galaxy formation or galaxies with an exotic metallicity/IMF (Schaerer 2002). The models of Schaerer (2003) and Raiter et al. (2010) have shown that the He II $\lambda$1640 line is a useful indicator to break the degeneracy between the stellar age and metallicity. This is due to the fact that the high excitation level of He II, $h\nu = 54.4$ eV, can be achieved only by massive stars with extremely low metallicities ($Z \sim 0$–$5 \times 10^{-6}$ Z$_\odot$). These models predict that galaxies hosting zero-metallicity stars (Population III stars, hereafter Pop III) can emit He II whose rest-frame EW, EW$_0$(He II), is up to a few times 10 Å. The UV continuum slope ($\beta$), defined as $f_\lambda \propto \lambda^\beta$, is also powerful to place constraints on the stellar age and metallicity because the $\beta$ value ranges to as low as $\gtrsim -3.0$ depending on the stellar age and metallicity (Schaerer 2003; Raiter et al. 2010). Therefore, it is important to simultaneously examine EW$_0$(Ly$\alpha$), EW$_0$(He II), and $\beta$ values to put constraints on stellar ages and metallicities of large EW$_0$(Ly$\alpha$) LAEs.

There are two problems in previous large EW$_0$(Ly$\alpha$) LAE studies. First, EW$_0$(Ly$\alpha$) measurements have large uncertainties. Because LAEs are generally faint in continua, it is difficult to measure the continuum flux at 1216 Å from spectroscopic data. Thus, most LAE studies have estimated the continuum flux at 1216 Å from photometric data in the wavelength range redwards of 1216 Å. Furthermore, previous studies have assumed the flat UV continuum slope, $\beta = -2.0$, to estimate the continuum flux at 1216 Å. Since large EW$_0$(Ly$\alpha$) LAEs are typically very faint in the continuum (Ando et al. 2006), large uncertainties remain in EW$_0$(Ly$\alpha$) values even if the continuum fluxes at 1216 Å are derived from photometric data. Secondly, detailed physical properties of large EW$_0$(Ly$\alpha$) LAEs have been scarcely investigated. There are no studies which placed constraints on stellar ages and metallicities of large EW$_0$(Ly$\alpha$) LAEs based on EW$_0$(Ly$\alpha$), EW$_0$(He II), and $\beta$ values. Kashikawa et al. (2012) have examined the stellar age and metallicity of a large EW$_0$(Ly$\alpha$) LAE at $z \sim 6.5$ based on EW$_0$(Ly$\alpha$) and EW$_0$(He II) values. However, the result is practically based on the EW$_0$(Ly$\alpha$) value because the EW$_0$(He II) value is only an upper limit.

In this study, we examine physical properties of six large EW$_0$(Ly$\alpha$) LAEs which are spectroscopically confirmed at $z \sim 2$. By modelling deep far-ultraviolet (FUV) photometric data with no a priori assumption on $\beta$, we carefully estimate EW$_0$(Ly$\alpha$) and $\beta$ values of our LAEs. Remarkably, we find that our LAEs have large EW$_0$(Ly$\alpha$) values ranging from 160 to 357 Å with a mean value of $252 \pm 30$ Å. The $\beta$ values of our LAEs vary from 1.6 to $-2.9$ with a small median value of $-2.5 \pm 0.2$. In order to place constraints on stellar ages and metallicities of our large EW$_0$(Ly$\alpha$) LAEs, we compare observational constraints of the large EW$_0$(Ly$\alpha$), the small $\beta$, and EW$_0$(He II) with theoretical models of Schaerer (2003) and Raiter et al. (2010). Since these theoretical models have fine metallicity grids at the low-metallicity range, we can investigate stellar ages and metallicities of our large EW$_0$(Ly$\alpha$) LAEs in detail. We also derive physical quantities such as the stellar mass ($M_\star$), the star formation rate (SFR), the full width at half-maximum, FWHM, of the Ly$\alpha$ lines, and the Ly$\alpha$ escape fraction ($f_{\rm esc}^{\rm Ly\alpha}$) from the spectral data and photometric data (Spectral Energy Distribution fitting; hereafter SED fitting).

This paper is organized as follows. We describe our large EW$_0$(Ly$\alpha$) LAE sample and data in Section 2. In Section 3, we derive EW$_0$(Ly$\alpha$) and $\beta$ values as well as several observational quantities of our LAEs. A discussion in the context of physical properties of large EW$_0$(Ly$\alpha$) LAEs is given in Section 4, followed by conclusions in Section 5. Throughout this paper, magnitudes are given in the AB system (Oke & Gunn 1983), and we assume a $\Lambda$ cold dark matter cosmology with $\Omega_{\rm m} = 0.3$, $\Omega_\Lambda = 0.7$, and $H_0 = 70$ km s$^{-1}$ Mpc$^{-1}$.

## 2 SAMPLE AND DATA

### 2.1 Large EW$_0$(Ly$\alpha$) LAE sample

Our large EW$_0$(Ly$\alpha$) LAEs are taken from the largest ($N \sim 3000$) parent LAE sample at $z \sim 2.2$ spanning in the COSMOS field, the *Chandra Deep Field*-South (CDFS), and the Subaru/*XMM–Newton* Deep Survey (SXDS; Nakajima et al. 2012, 2013; Konno et al. 2016; Kusakabe et al., in preparation). The parent sample is based on Subaru/Suprime-Cam imaging observations with our custom-made narrow-band filter, *NB*387. The central wavelength and the FWHM of *NB*387 are 3870 Å and 94 Å, respectively. The parent LAE sample has been selected by the following colour criteria:

$$u^* - NB387 > 0.5 \text{ and } B - NB387 > 0.2, \quad (1)$$

satisfying the condition that the EW$_0$(Ly$\alpha$) value should be larger than 30 Å. The parent sample has been used to examine LAEs' metal abundances and ionization parameters (Nakajima et al. 2012, 2013; Nakajima & Ouchi 2014), kinematics of the interstellar medium (ISM; Hashimoto et al. 2013, 2015; Shibuya et al. 2014b), diffuse Ly$\alpha$ haloes (Momose et al. 2014, 2016), morphologies (Shibuya et al. 2014a), dust properties (Kusakabe et al. 2015), and the Ly$\alpha$ luminosity function (Konno et al. 2016).

From the parent sample, we use six objects with strong *NB*387 excesses,

$$u^* - NB387 > 1.0 \text{ and } B - NB387 > 1.4, \quad (2)$$

as well as Ly$\alpha$ identifications which are listed in Table 1: four from the COSMOS field, COSMOS-08501, COSMOS-40792, COSMOS-41547, and COSMOS-44993, and two from the SXDS-centre (SXDS-C) field, SXDS-C-10535 and SXDS-C-16564. Since our targets are large EW$_0$(Ly$\alpha$) objects whose Ly$\alpha$ emission originates from star-forming activities, we examine if our sample includes a Ly$\alpha$ blob (LAB; Møller & Warren 1998; Steidel et al. 2000). This is because Ly$\alpha$ emission of LABs is thought to be powered by AGN activities (e.g. Haiman & Rees 2001), superwinds from starburst galaxies (e.g. Taniguchi & Shioya 2000), and cold accretion (e.g. Haiman, Spaans & Quataert 2000). To check the presence of LABs, we have inspected the isophotal areas of *NB*387 images which trace the Ly$\alpha$ morphologies. We have obtained 4.2 arcsec$^2$ (COSMOS-08501), 1.1 arcsec$^2$ (COSMOS-40792), 1.7 arcsec$^2$ (COSMOS-41547), 1.5 arcsec$^2$ (COSMOS-44993), 1.7 arcsec$^2$ (SXDS-C-10535), and 6.2 arcsec$^2$ (SXDS-C-16564). These isophotal areas correspond to the radii of 9–21 kpc at $z \sim 2.2$. These radii are spatially compact compared to the half-light radii of typical $z \sim 3$ LABs, 30–300 kpc (Steidel et al. 2000; Matsuda et al. 2004). Thus, we conclude that our large EW$_0$(Ly$\alpha$) LAEs do not include a LAB.

### 2.2 Photometric data

We performed photometry using SEXTRACTOR (Bertin & Arnouts 1996). We use 14 bandpasses: $u^*$, *NB*387, $B$, $V$, $r'$, $i'$, and $z'$ data taken with Subaru/Suprime-Cam, $J$ data taken with United Kingdom Infrared Telescope (UKIRT)/WFCAM, $H$ and

**Table 1.** Sample of large EW$_0$(Ly$\alpha$) LAEs. (1) Object ID; (2) and (3) right ascension and declination; (4) and (5) $u^* - NB387$ and $B - NB387$ colours; (6) spectroscopically identified line(s) and instruments used for observations; (7) redshifts inferred from the Ly$\alpha$ lines; and (8) source of the information.

| Object (1) | $\alpha$(J2000) (2) | $\delta$(J2000) (3) | $u^* - NB387$ (4) | $B - NB387$ (5) | Line (6) | $z_{Ly\alpha}$ (7) | Source[a] (8) |
|---|---|---|---|---|---|---|---|
| COSMOS-08501 | 10:01:16.80 | +02:05:36.3 | 1.45 | 2.17 | Ly$\alpha$ (MagE), H$\alpha$ (NIRSPEC) | 2.162 | N13, H15 |
| COSMOS-40792 | 09:59:46.66 | +02:24:34.2 | 1.44 | 2.02 | Ly$\alpha$ (LRIS) | 2.209 | S14 |
| COSMOS-41547 | 09:59:41.91 | +02:25:00.0 | 1.00 | 1.90 | Ly$\alpha$ (LRIS) | 2.152 | S14 |
| COSMOS-44993 | 09:59:53.87 | +02:27:11.0 | 1.42 | 1.48 | Ly$\alpha$ (LRIS) | 2.214 | S14 |
| SXDS-C-10535 | 02:17:41.92 | −05:02:55.9 | 1.11 | 1.42 | Ly$\alpha$ (LRIS) | 2.213 | S14 |
| SXDS-C-16564 | 02:19:09:54 | −04:57:13.3 | 1.46 | 1.95 | Ly$\alpha$ (IMACS) | 2.176 | N12 |

*Note.*[a]N12: Nakajima et al. (2012); N13: Nakajima et al. (2013); S14: Shibuya et al. (2014b); H15: Hashimoto et al. (2015).

**Table 2.** Photometry of our LAEs. All magnitudes are total magnitudes. 99.99 mag indicates a negative flux density. Magnitudes in parentheses are 1$\sigma$ uncertainties.

| Object | $u^*$ | $NB387$ | $B$ | $V$ | $r'$ | $i'$ | $z'$ | $J$ | $H$ | $K_s$ | [3.6] | [4.5] | [5.8] | [8.0] |
|---|---|---|---|---|---|---|---|---|---|---|---|---|---|---|
| COSMOS | | | | | | | | | | | | | | |
| 08501 | 25.14 | 23.69 | 25.86 | 25.91 | 26.05 | 25.96 | 25.77 | 99.99 | 26.47 | 25.85 | 99.99 | 99.99 | 99.99 | 99.99 |
| | (0.03) | (0.03) | (0.05) | (0.17) | (0.16) | (0.20) | (0.52) | (–) | (1.39) | (1.00) | (–) | (–) | (–) | (–) |
| 40792 | 26.72 | 25.28 | 27.30 | 27.14 | 27.94 | 31.21 | 27.41 | 99.99 | 99.99 | 99.99 | 25.54 | 25.79 | 99.99 | 99.99 |
| | (0.14) | (0.12) | (0.21) | (0.56) | (1.38) | (3.38) | (0.62) | (–) | (–) | (–) | (1.45) | (1.00) | (–) | (–) |
| 41547 | 26.06 | 25.07 | 26.97 | 26.59 | 26.70 | 26.21 | 27.46 | 99.99 | 25.71 | 24.94 | 99.99 | 99.99 | 22.50 | 22.72 |
| | (0.08) | (0.10) | (0.15) | (0.32) | (0.30) | (0.25) | (0.68) | (–) | (0.66) | (1.42) | (–) | (–) | (0.62) | (2.18) |
| 44993 | 26.50 | 25.08 | 26.56 | 27.02 | 26.71 | 26.55 | 27.41 | 24.54 | 99.99 | 25.52 | 99.99 | 99.99 | 99.99 | 99.99 |
| | (0.12) | (0.10) | (0.10) | (0.49) | (0.31) | (0.35) | (0.62) | (1.35) | (–) | (0.60) | (–) | (–) | (–) | (–) |
| Offset[a] | − 0.16 | 0.00 | 0.03 | 0.23 | 0.20 | 0.12 | 0.21 | 0.08 | 0.07 | 0.07 | −0.02 | 0.03 | 0.05 | 0.12 |
| SXDS-C | | | | | | | | | | | | | | |
| 10535 | 25.84 | 24.73 | 26.15 | 26.29 | 26.64 | 26.61 | 26.94 | 27.12 | 27.54 | 25.64 | 25.92 | 99.99 | 99.99 | 99.99 |
| | (0.08) | (0.10) | (0.08) | (0.12) | (0.22) | (0.22) | (0.83) | (0.62) | (1.78) | (0.72) | (1.45) | (–) | (–) | (–) |
| 16564 | 24.14 | 22.68 | 24.63 | 24.83 | 24.97 | 25.09 | 25.16 | 25.18 | 23.83 | 24.40 | 25.49 | 29.91 | 99.99 | 99.99 |
| | (0.02) | (0.01) | (0.02) | (0.03) | (0.05) | (0.05) | (0.14) | (0.37) | (0.19) | (0.20) | (1.11) | (4.24) | (–) | (–) |
| Offset[a] | − 0.25 | 0.00 | 0.03 | 0.06 | 0.18 | 0.25 | 0.18 | −0.01 | −0.06 | −0.06 | −0.05 | 0.00 | −0.15 | −0.15 |

*Note.* [a]Zero-point magnitude offsets quoted from Skelton et al. (2014).

$K$ data taken with Canada–France–Hawaii Telescope/WIRCAM (UKIRT/WFCAM) for COSMOS (SXDS-C), and *Spitzer*/IRAC 3.6, 4.5, 5.8, and 8.0 μm from the *Spitzer* legacy survey of the UDS fields.

For the detailed procedure of photometry, we refer the reader to Nakajima et al. (2012). Recently, Skelton et al. (2014) have re-calibrated zero-point magnitudes for the COSMOS and SXDS fields using 3D-HST (Brammer et al. 2012) and CANDELS (Grogin et al. 2011; Koekemoer et al. 2011) data. Skelton et al. (2014) have found that the zero-point magnitude offsets are from 0.00 to −0.25. For secure estimates of physical quantities, we correct our zero-point magnitudes for the offsets listed in tables 11 and 12 of Skelton et al. (2014). Table 2 summarizes the photometry of our objects.

### 2.3 Spectroscopic data

We carried out optical observations with Magellan/IMACS (PI: M. Ouchi), Magellan/MagE (PI: M. Rauch), and Keck/LRIS (PI: M. Ouchi). Details of the observations and data reduction procedures have been presented in Nakajima et al. (2012, IMACS), Shibuya et al. (2014b, LRIS), and Hashimoto et al. (2015, MagE). The spectral resolutions for our observations were $R \sim 700$ (IMACS), ∼1100 (LRIS), and ∼4100 (MagE). SXDS-C-16564 was observed with IMACS, from which we identified the Ly$\alpha$ line (Nakajima et al. 2012). COSMOS-40792, COSMOS-41547, COSMOS-44933, and SXDS-C-10535 were observed with LRIS. Although these LAEs are as faint as $B \sim$ 26–27, we detected the Ly$\alpha$ lines due to the high sensitivity of LRIS (Shibuya et al. 2014b). COSMOS-08501 was observed with MagE, from which we identified the Ly$\alpha$ line (Hashimoto et al. 2015). The H$\alpha$ line was also detected in COSMOS-08501 with Keck/NIRSPEC at the significance level of ∼5$\sigma$ (Nakajima et al. 2013).

We additionally search for the C IV λ1549 and He II λ1640 lines in our LAEs. We determine a line to be detected, if there exists an emission line above the 3$\sigma$ sky noise around the wavelength expected from the Ly$\alpha$ redshift. In this analysis, we measure the sky noise from the spectrum within 50 Å from the line wavelength. Neither C IV nor He II was detected above 3$\sigma$ in our LAEs. The flux upper limits of C IV are used to diagnose signatures of AGN in our LAEs (Section 2.4), while those of He II enable us to place constraints on the stellar ages and metallicities of our LAEs (Section 4.3). Fig. 1 shows 1D spectra corresponding to data around Ly$\alpha$, C IV, He II, and H$\alpha$ lines.

### 2.4 AGN activities in the sample

We examine whether our LAEs host an AGN in three ways. First, we compare the sky coordinates of the objects with those in very deep archival X-ray and radio catalogues (Elvis et al. 2009). The sensitivity limits are $1.9 \times 19^{-16}$ (0.5–2.0 keV band), $7.3 \times 19^{-16}$ (2–10 keV band), and $5.7 \times 19^{-16}$ erg cm$^{-2}$ s$^{-1}$ (0.5–10 keV band).

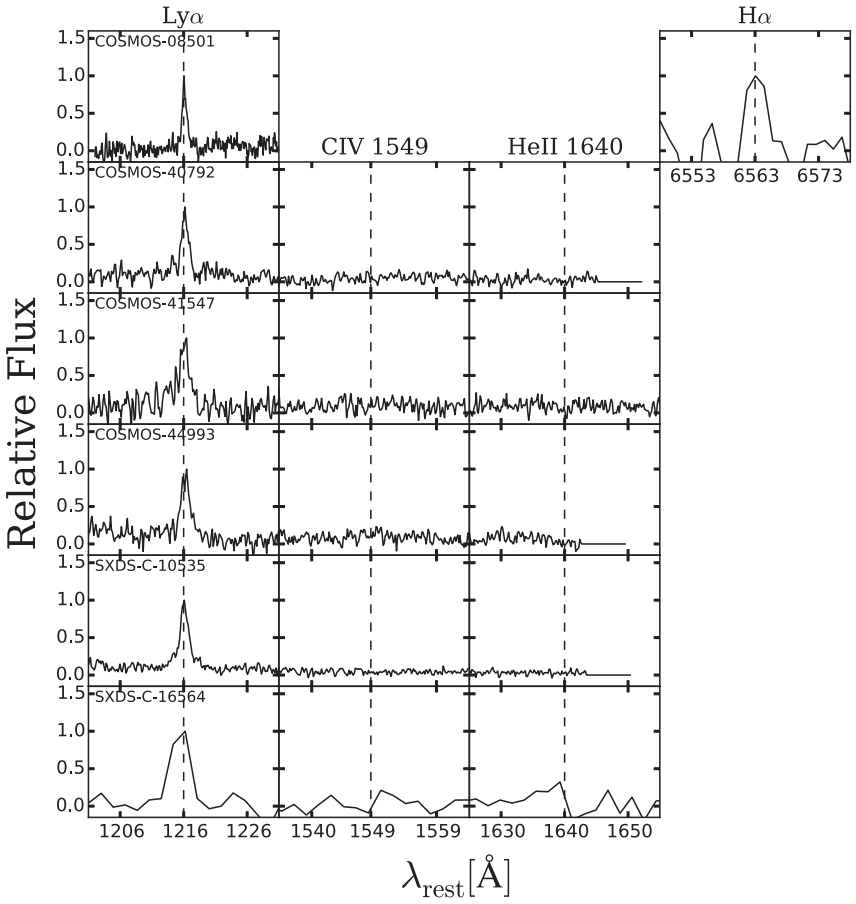


**Figure 1.** From left to right, reduced 1D spectra corresponding to wavelength regions near Ly$\alpha$, C IV $\lambda$1549, He II $\lambda$1640, and H$\alpha$ of our LAEs. The dashed lines in the 1D spectra show the expected locations of the lines.

We also refer to the radio catalogue constructed by Schinnerer et al. (2010). No counterpart for the LAEs is found in any of the catalogues.

Secondly, we search for the C IV 1549 line whose high-ionization potential can be achieved by AGN activities. The C IV line is not detected on an individual basis (Section 2.3). To obtain a strong constraint on the presence of an AGN, we stack the four LRIS spectra by shifting individual spectral data from the observed to the rest frame. We infer the systemic redshifts of the four LRIS objects as follows. The Ly$\alpha$ line is known to be redshifted with respect to the systemic redshift by 200–400 km s$^{-1}$ (e.g. Steidel et al. 2010; Hashimoto et al. 2013; Erb et al. 2014; Shibuya et al. 2014b; Henry et al. 2015; Stark et al. 2015). Based on an anti-correlation between the Ly$\alpha$ velocity offset and EW$_0$(Ly$\alpha$) (Hashimoto et al. 2013; Erb et al. 2014; Shibuya et al. 2014b), we assume that our large EW$_0$(Ly$\alpha$) LAEs have the same Ly$\alpha$ velocity offsets as COSMOS-08501, 82 $\pm$ 40 km s$^{-1}$ (Hashimoto et al. 2015). Fig. 2 shows the stacked FUV spectrum of the four LRIS spectra. The C IV line is not detected even in the composite spectrum. We obtain the 3$\sigma$ lower limit of the flux ratio, $f_{\rm Ly\alpha}/f_{\rm CIV} > 19.0$, where $f_{\rm Ly\alpha}$ and $f_{\rm CIV}$ are the Ly$\alpha$ and C IV fluxes, respectively. The flux ratio is significantly larger than that for $z \sim$ 2–3 radio galaxies, $f_{\rm Ly\alpha}/f_{\rm CIV} = 6.9$ (Villar-Martín et al. 2007).

Finally, Nakajima et al. (2013) have examined the position of COSMOS-08501 in the BPT diagram (Baldwin, Phillips & Terlevich 1981). As shown in fig. 3 of Nakajima et al. (2013), the upper limit of the flux ratio of [N II] $\lambda$6584 to H$\alpha$, log([N II] $\lambda$6584/H$\alpha$) $\lesssim -0.7$, indicates that COSMOS-08501 does not host an AGN.

Thus, we conclude that no AGN activity is seen in our LAEs.

## 3 RESULTS

### 3.1 SED fitting

We perform stellar population synthesis model fitting to our LAEs to derive the stellar mass ($M_\star$), stellar dust extinction ($E(B-V)_\star$), the stellar age, and the SFR. For the detailed procedure, we refer the reader to Ono et al. (2010a,b). Briefly, we use the stellar population synthesis model of GALAXEV (Bruzual & Charlot 2003) including nebular emission (Schaerer & de Barros 2009), and adopt the Salpeter IMF (Salpeter 1955). For simplicity, we use constant star formation models. Indeed, several authors have assumed the constant star formation history (SFH) for LAE studies at $z \sim 2$ (e.g. Kusakabe et al. 2015; Hagen et al. 2016) and at $z > 3$ (see table 6 in Ono et al. 2010a). Because LAEs are metal-poor star-forming galaxies (Finkelstein et al. 2011; Nakajima et al. 2012, 2013; Song et al. 2014), we choose a metallicity of $Z = 0.2\,Z_\odot$. We use Calzetti's law (Calzetti et al. 2000) for $E(B-V)_\star$, and apply 18 per cent inter galactic medium (IGM) attenuation of continuum photons shortwards of Ly$\alpha$ using the prescription of Madau (1995). To derive the best-fitting parameters, we use all bandpasses mentioned in Section 2.2 except for $u^*$- and *NB*387-band data. Neither $u^*$- nor *NB*387-band data have been used since the photometry of these

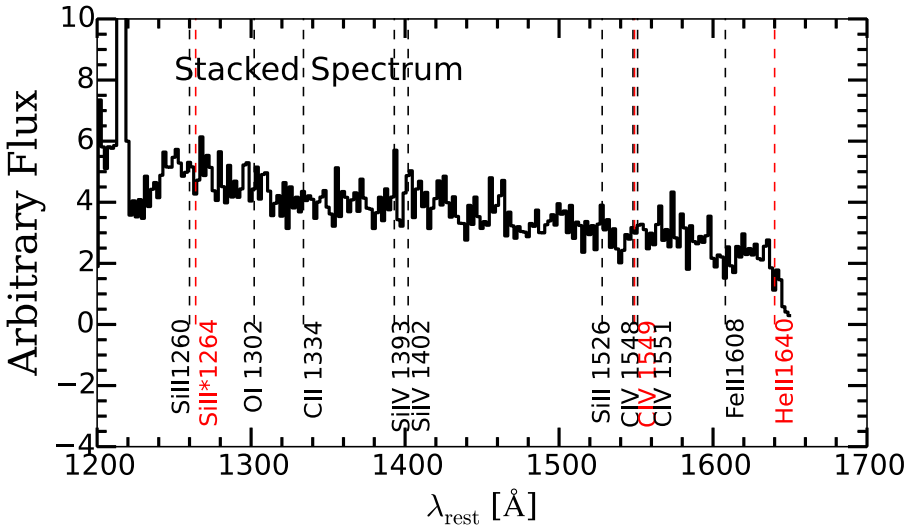


**Figure 2.** Composite rest-frame UV spectrum of the four LRIS spectra. The black and red vertical dashed lines indicate wavelengths of interstellar absorption lines and emission lines, respectively.

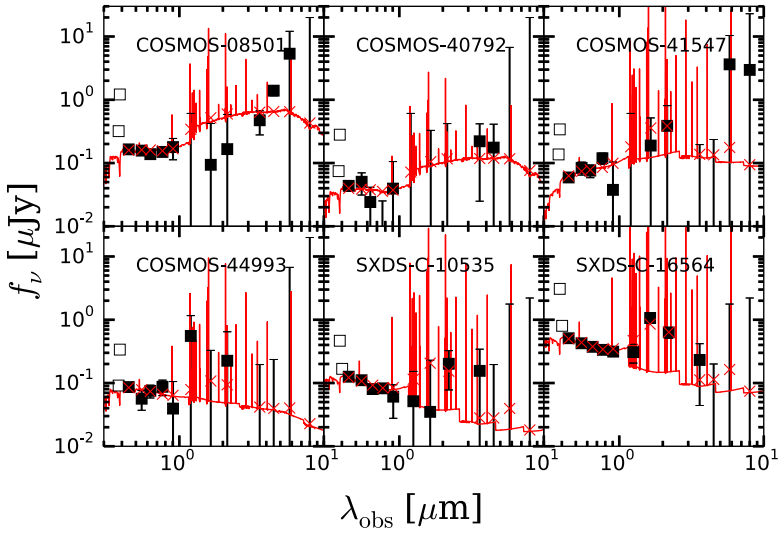


**Figure 3.** Results of SED fitting for our LAEs. The filled squares denote the photometry points used for SED fitting, while the open squares are those omitted in SED fitting due to the contamination of Ly$\alpha$ emission and IGM absorption. The red lines represent the best-fitting model spectra, while the red crosses correspond to the flux densities at individual passbands expected from the best-fitting models.

bands is contaminated by IGM absorption and/or Ly$\alpha$ emission. Fig. 3 shows the best-fitting model spectra with the observed flux densities. The derived quantities and their 1$\sigma$ uncertainties are summarized in Table 3.

In Table 3, our LAEs have stellar masses mostly $M_\star = 10^{7-8}$ M$_\odot$ with a median value of $7.1^{+4.8}_{-2.8} \times 10^7$ M$_\odot$. The median value is smaller than that of $z \sim 2$ LAEs with small EW$_0$(Ly$\alpha$), 2–5 $\times$ $10^8$ M$_\odot$ (Nakajima et al. 2012; Hagen et al. 2016). Nilsson et al. (2011), Oteo et al. (2015), and Shimakawa et al. (2016) have also studied stellar masses of $z \sim 2$ LAEs. In these studies, there are no LAEs with $M_\star < 10^8$ M$_\odot$. These results indicate that our sample is consisted of low-mass LAEs.

The dust extinction of our LAEs varies from $E(B-V)_\star = 0.00$ to 0.25 with a median value of $0.02^{+0.04}_{-0.02}$. This is lower than the typical dust extinction of $z \sim 2$ LAEs, $E(B-V)_\star \sim 0.2$–0.3 (Guaita et al. 2011; Nakajima et al. 2012; Oteo et al. 2015). This result shows that our LAEs have small amounts of dust.

**Table 3.** Results of SED fitting. Stellar metallicity is fixed to 0.2 Z$_\odot$. (1) Object ID; (2) $\chi^2$ of the fitting; (3) stellar mass; (4) stellar dust extinction; (5) stellar age; and (6) star formation rate.

| Object | $\chi^2$ | log($M_*$) (M$_\odot$) | $E(B-V)_\star$ | log(age) (yr) | log(SFR) (M$_\odot$ yr$-$1) |
|---|---|---|---|---|---|
| (1) | (2) | (3) | (4) | (5) | (6) |
| COSMOS-8501 | 1.8 | $7.8^{+1.2}_{-0.3}$ | $0.08^{+0.04}_{-0.08}$ | $6.2^{+2.8}_{-1.1}$ | $1.68^{+1.24}_{-1.44}$ |
| COSMOS-40792 | 3.8 | $8.9^{+0.2}_{-2.1}$ | $0.00^{+0.10}_{-0.00}$ | $9.4^{+0.0}_{-4.4}$ | $-0.37^{+2.53}_{-0.00}$ |
| COSMOS-41547 | 4.8 | $8.1^{+0.4}_{-0.3}$ | $0.25^{+0.04}_{-0.07}$ | $6.9^{+0.8}_{-0.4}$ | $1.27^{+0.42}_{-0.51}$ |
| COSMOS-44993 | 3.1 | $7.6^{+1.2}_{-0.5}$ | $0.03^{+0.09}_{-0.03}$ | $7.4^{+1.6}_{-2.3}$ | $0.23^{+2.28}_{-0.28}$ |
| SXDS1-10535 | 3.4 | $7.3^{+0.5}_{-0.0}$ | $0.00^{+0.02}_{-0.00}$ | $6.5^{+1.2}_{-1.4}$ | $0.80^{+1.50}_{-0.59}$ |
| SXDS1-16564 | 9.2 | $7.9^{+0.0}_{-0.0}$ | $0.00^{+0.00}_{-0.00}$ | $6.5^{+0.1}_{-0.1}$ | $1.43^{+0.1}_{-0.1}$ |

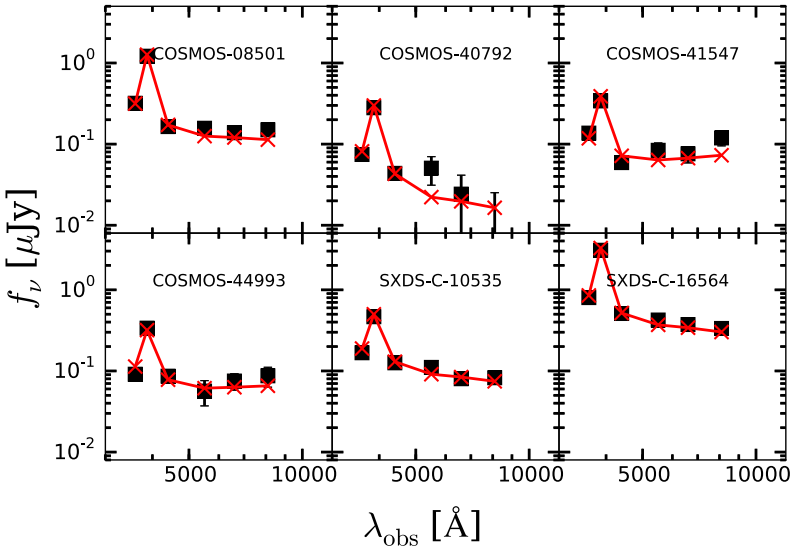


**Figure 4.** Rest-frame UV SEDs, from $u^*$- to $i'$-band data, of our LAEs. The filled squares denote the photometry used for the fits, while the red crosses correspond to the flux densities at individual passbands expected from the best-fitting models.

### 3.2 Careful estimates of EW$_0$(Ly$\alpha$) and $\beta$

We model a realistic FUV spectrum of a LAE to derive EW$_0$(Ly$\alpha$), the Ly$\alpha$ luminosity ($L$(Ly$\alpha$)), the UV absolute magnitude ($M_{\rm UV}$), and $\beta$. As mentioned in Section 1, EW$_0$(Ly$\alpha$) estimates in previous studies are based on several assumptions: (i) the UV continuum slope is flat, $\beta = -2.0$, and (ii) the passbands are ideal top-hat response functions (e.g. Malhotra & Rhoads 2002; Guaita et al. 2011; Mawatari et al. 2012). These factors add systematic uncertainties in EW$_0$(Ly$\alpha$).

In this work, the LAE spectrum is modelled as a combination of a delta-function Ly$\alpha$ line and a linear continuum,

$$f_{\nu,{\rm Ly}\alpha} = F({\rm Ly}\alpha) \times \delta(\nu - \nu_{{\rm Ly}\alpha}), \tag{3}$$

$$f_{\nu,{\rm cont}} = A \times \nu^{-(\beta_{1200-2800}+2)}, \tag{4}$$

where $f_{\nu,\,{\rm Ly}\alpha}$ ($f_{\nu,\,{\rm cont}}$) is the Ly$\alpha$ (continuum) flux per unit frequency in erg cm$^{-2}$ s$^{-1}$ Hz$^{-1}$, while $F$(Ly$\alpha$) is the integrated flux of the line in erg cm$^{-2}$ s$^{-1}$. The function $\delta(\nu - \nu_{{\rm Ly}\alpha})$ is a delta function, and the function $A$ corresponds to the amplitude of the continuum flux. In equation (4), $A$ is expressed as

$$A = (2.0 \times 10^{15})^{\beta_{1200-2800}+2} \times 10^{-0.4(m_{1500}+48.6)}, \tag{5}$$

where $\beta_{1200-2800}$ is the UV continuum slope in the rest-frame wavelength range of 1200–2800 Å, while $m_{1500}$ indicates the apparent magnitude at 1500 Å. With $f_{\nu,\,{\rm cont}}$ and $F$(Ly$\alpha$) in equations (3) and (4), the modelled flux in the $i$th band is defined as

$$f^{(i)}_{\nu,{\rm model}} = \frac{\int f_\nu T^{(i)}_\nu {\rm d}\nu}{\int T^{(i)}_\nu {\rm d}\nu} \tag{6}$$

$$= \frac{\int_{\nu_{\rm s}}^{\nu_{{\rm Ly}\alpha}} f_{\nu,{\rm cont}} T^{(i)}_\nu {\rm d}\nu + F({\rm Ly}\alpha) T^{(i)}_{\nu,{\rm Ly}\alpha} + \alpha \int_{\nu_{{\rm Ly}\alpha}}^{\nu_{\rm e}} f_{\nu,{\rm cont}} T^{(i)}_\nu {\rm d}\nu}{\int_{\nu_{\rm s}}^{\nu_{\rm e}} T^{(i)}_\nu {\rm d}\nu}. \tag{7}$$

In equation (7), $T^{(i)}_\nu$ is the response curve of the $i$th band. The constants of $\nu_{\rm s}$ and $\nu_{\rm e}$ indicate the frequencies corresponding to the upper and lower ends of the response curves, respectively. The constant $T^{(i)}_{\nu,{\rm Ly}\alpha}$ is the response curve value of the $i$th band at the Ly$\alpha$ frequency, $\nu_{{\rm Ly}\alpha}$, where $\nu_{{\rm Ly}\alpha}$ is calculated from the Ly$\alpha$ redshift, $z_{{\rm Ly}\alpha}$ (Table 1). Finally, $\alpha$ means the continuum photon transmission shortwards of Ly$\alpha$ after the IGM absorption. Using the prescription of Madau (1995), at $z \simeq 2$, it is

$$\alpha = \begin{cases} 0.82 & (\nu \geq \nu_{{\rm Ly}\alpha}) \\ 1.0 & (\nu < \nu_{{\rm Ly}\alpha}). \end{cases}$$

To estimate EW$_0$(Ly$\alpha$) and other quantities, we compare the modelled flux in the $i$th band with the observed one in the $i$th band. The observed flux in the $i$th band is expressed as

$$f^{(i)}_{\nu,{\rm obs}} = 10^{-0.4({\rm AB}^{(i)}+48.6)}, \tag{8}$$

where AB$^{(i)}$ is the AB magnitude of the $i$th band listed in Table 2. For each LAE, we use six rest-frame FUV data, from $u^*$ to $i'$ band. With equations (7) and (8), we search for the best-fitting spectrum which minimizes

$$\chi^2 = \sum_i^6 \frac{\left\{ f^{(i)}_{\nu,{\rm obs}} - f^{(i)}_{\nu,{\rm model}} \left[ F({\rm Ly}\alpha), \beta_{1200-2800}, m_{1500} \right] \right\}^2}{\sigma^2 \left[ f^{(i)}_{\nu,{\rm obs}} \right]}, \tag{9}$$

where $\sigma \left[ f^{(i)}_{\nu,{\rm obs}} \right]$ is the photometric and systematic errors in the $i$th bandpass. The uncertainties in the best-fitting parameters correspond to the $1\sigma$ confidence interval, $\Delta\chi^2 < 1.0$. With best-fitting parameters of $\beta_{1200-2800}$ and $m_{1500}$, we obtain $f_{\nu,\,{\rm cont}}$ from equations (4) and (5). The flux $f_{\nu,\,{\rm cont}}$ is then converted into $f_{\lambda,\,{\rm cont}}$ from the relation

$$f_{\lambda,{\rm cont}} = \frac{c}{\lambda^2} \times f_{\nu,{\rm cont}}, \tag{10}$$

where $c$ is the speed of light. Using equation (10), we derive the continuum flux at 1216 Å, $f_{{\rm cont},\,1216}$, to obtain EW$_0$(Ly$\alpha$) as

$${\rm EW}_0({\rm Ly}\alpha) = \frac{F({\rm Ly}\alpha)}{f_{{\rm cont},1216}} \times \frac{1}{1+z_{{\rm Ly}\alpha}}. \tag{11}$$

We obtain $M_{\rm UV}$ from the continuum flux at 1500 Å, $f_{{\rm cont},\,1500}$, as below:

$$M_{\rm UV} = m_{1500} - 5\log(d_{\rm L}/10{\rm pc}) + 2.5\log(1+z_{{\rm Ly}\alpha}), \tag{12}$$

where $d_{\rm L}$ indicates the luminosity distance corresponding to $z_{{\rm Ly}\alpha}$.

Fig. 4 shows the best-fitting model spectra. As can be seen, our technique reproduces the rest-frame UV SEDs. The best-fitting

**Table 4.** Results of careful estimates of EW$_0$(Ly$\alpha$) and $\beta$. (1) Object ID; (2) $\chi^2$ of the fitting; (3) and (4) rest-frame Ly$\alpha$ EW and Ly$\alpha$ luminosity; (5) UV absolute magnitude; and (6) UV spectral slope at the rest-frame wavelength range of 1800–2200 Å.

| Object | $\chi^2$ | EW$_0$(Ly$\alpha$) (Å) | $L$(Ly$\alpha$) ($10^{42}$ erg s$^{-1}$) | $M_{\rm UV}$ | $\beta_{1200-2800}$ |
|---|---|---|---|---|---|
| (1) | (2) | (3) | (4) | (5) | (6) |
| COSMOS-8501 | 8.5 | $284^{+39}_{-16}$ | $8.9^{+0.8}_{-0.5}$ | $-18.0^{+0.1}_{-0.1}$ | $-2.3^{+0.3}_{-0.1}$ |
| COSMOS-40792 | 2.3 | $357^{+96}_{-114}$ | $2.5^{+0.3}_{-0.4}$ | $-17.0^{+0.5}_{-0.3}$ | $-2.9^{+1.0}_{-1.1}$ |
| COSMOS-41547 | 13.5 | $303^{+59}_{-46}$ | $3.3^{+0.3}_{-0.4}$ | $-17.9^{+0.2}_{-0.2}$ | $-1.6^{+0.2}_{-0.2}$ |
| COSMOS-44993 | 2.3 | $215^{+115}_{-22}$ | $2.9^{+0.8}_{-0.4}$ | $-18.0^{+0.3}_{-0.1}$ | $-1.8^{+0.3}_{-0.4}$ |
| SXDS-C-10535 | 5.8 | $160^{+12}_{-16}$ | $4.1^{+0.4}_{-0.8}$ | $-18.5^{+0.1}_{-0.1}$ | $-2.6^{+0.1}_{-0.1}$ |
| SXDS-C-16564 | 18.7 | $195^{+7}_{-8}$ | $20.0^{+1.2}_{-1.5}$ | $-20.0^{+0.1}_{-0.1}$ | $-2.6^{+0.1}_{-0.1}$ |

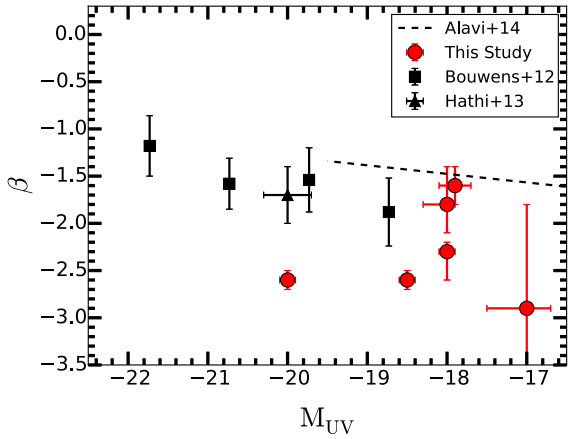


**Figure 5.** UV spectral slope ($\beta$) as a function of the absolute UV magnitude at 1500 Å ($M_{\rm UV}$) at $z \sim 2$. The red circles are our LAEs, where we adopt $\beta_{1200-2800}$ as the $\beta$ values. The dashed line is the best linear fit for $z \sim 2$ lensed LBGs (Alavi et al. 2014), while the black triangle is the average value of $z \sim 2$ LBGs (Hathi et al. 2013). The black squares indicate $z \sim 2$ LBGs studied by Bouwens et al. (2009), where error bars denote the $1\sigma$ of the distribution at each magnitude bin.

parameters and their $1\sigma$ uncertainties are summarized in Table 4. In Table 4, we find that our LAEs have large EW$_0$(Ly$\alpha$) values ranging from 160 to 357 Å with a mean value of $252 \pm 30$ Å. We confirm that LAEs with EW$_0$(Ly$\alpha$) $\gtrsim$ 200 Å exist by our fitting method with no a priori assumption on UV continuum slopes. UV continuum slopes vary from $\beta_{1200-2800} = -1.6$ to $-2.9$ with small mean and median values of $-2.3 \pm 0.2$ and $-2.5 \pm 0.2$, respectively. The median Ly$\alpha$ luminosity of our LAEs is $L(\mathrm{Ly}\alpha) = 3.7^{+2.8}_{-2.8} \times 10^{42}$ erg s$^{-1}$. This is broadly consistent with the characteristic Ly$\alpha$ luminosity of $z \sim 2$ LAEs obtained by Hayes et al. (2010), Ciardullo et al. (2012), and Konno et al. (2016). The median UV absolute magnitude of our LAEs is $M_{\rm UV} = -18.5$. Fig. 5 plots $\beta$ against $M_{\rm UV}$ for our LAEs and Lyman-break galaxies (LBGs) at $z \sim 2$ (Bouwens et al. 2009; Hathi et al. 2013; Alavi et al. 2014). We note that the error bar of the data points of Bouwens et al. (2009) indicates the $1\sigma$ of the $\beta$ distribution at each magnitude bin. In Fig. 5, our LAEs have $\beta$ values comparable to or smaller than the LBGs at a given $M_{\rm UV}$ value, implying that large EW$_0$(Ly$\alpha$) objects have small UV continuum slopes. This trend is consistent with previous results (e.g. Stark et al. 2010; Hathi et al. 2016).

In Section 4.3, we constrain the stellar ages and metallicities of our LAEs based on comparisons of the EW$_0$(Ly$\alpha$) and UV

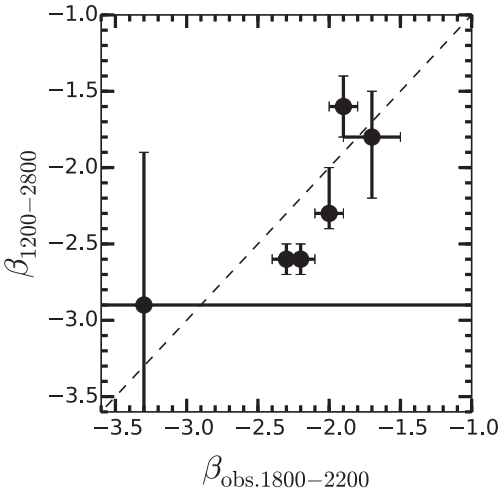


**Figure 6.** Comparison of the two UV continuum slopes, $\beta_{1200-2800}$ and $\beta_{\rm obs.1800-2200}$, for our LAEs. The dashed line indicates the one-to-one relation.

continuum slopes with stellar evolution models of Schaerer (2003) and Raiter et al. (2010). Although we have estimated UV continuum slopes at the wavelength range of 1200–2800 Å, Schaerer (2003) and Raiter et al. (2010) have computed UV continuum slopes at the wavelength range of 1800–2200 Å. Thus, we also calculate UV continuum slopes of our LAEs at the same wavelength range, $\beta_{\rm obs.1800-2200}$, with the following equation:

$$\beta_{\rm obs.1800-2200} = -\frac{V - (r' + i')/2}{2.5\log(\lambda_V/(\lambda_{r'} + \lambda_{i'})/2)} - 2, \quad (13)$$

where $V$, $r'$, and $i'$ are the magnitudes listed in Table 2, while $\lambda_V$, $\lambda_{r'}$, and $\lambda_{i'}$ correspond to the central wavelengths of each band, 5500, 6300, and 7700 Å, respectively. We obtain $\beta_{\rm obs.1800-2200} = -2.0 \pm 0.1$ (COSMOS-08501), $-3.3 \pm 4.0$ (COSMOS-40792), $-1.9 \pm 0.1$ (COSMOS-41547), $-1.7 \pm 0.2$ (COSMOS-44993), $-2.3 \pm 0.1$ (SXDS-C-10535), and $-2.2 \pm 0.1$ (SXDS-C-16564). Fig. 6 plots $\beta_{1200-2800}$ against $\beta_{\rm obs.1800-2200}$. The data points lie on the one-to-one relation, showing that the two UV continuum slopes are consistent with each other.

We note here that the models of Schaerer (2003) and Raiter et al. (2010) do not take into account dust extinction effects on UV continuum slopes. For fair comparisons, we derive the intrinsic UV continuum slopes, $\beta_{1800-2200}$. We find that UV continuum slopes increase by 0.5 for $E(B-V)_\star = 0.1$ based on a combination of the empirical relation, $A_{1600} = 4.43 + 1.99\beta$ (Meurer, Heckman & Calzetti 1999), and Calzetti extinction, $A_{1600} = k_{1600}E(B-V)_\star$ ($k_{1600} = 10$; Ouchi et al. 2004). With $E(B-V)_\star$ in Table 3, we obtain $\beta_{1800-2200} = -2.4^{+0.2}_{-0.4}$ (COSMOS-08501), $-3.3^{+7.9}_{-7.9}$ (COSMOS-40792), $-3.1^{+0.3}_{-0.4}$ (COSMOS-41547), $-1.9^{+0.6}_{-0.4}$ (COSMOS-44993), $-2.3^{+0.1}_{-0.1}$ (SXDS-C-10535), and $-2.2^{+0.1}_{-0.1}$ (SXDS-C-16564). In this calculation, we have adopted $2\sigma$ errors in $\beta_{\rm obs.1800-2200}$ to obtain conservative uncertainties in $\beta_{1800-2200}$. The mean and median correction factors are as small as $-0.3 \pm 0.2$ and $-0.1 \pm 0.2$, respectively. This is due to the fact that our LAEs have the low median stellar dust extinction value, $E(B-V)_* = 0.02^{+0.04}_{-0.02}$. One might be concerned about the systematic uncertainty of using two different models; we have adopted the model of GALAXEV to derive stellar dust extinction and the correction factors for UV continuum slopes, whereas we use the models of Schaerer (2003) and Raiter et al. (2010) to compare with $\beta_{1800-2200}$. However, the systematic uncertainty is negligibly small because our LAEs have small $\beta_{\rm obs.1800-2200}$

**Table 5.** Summary of spectroscopic properties of our large $EW_0(Ly\alpha)$ LAEs. (1) Object ID; (2) FWHMs of the Ly$\alpha$ lines corrected for the instrumental resolutions; (3) 3$\sigma$ upper limits of the flux ratio of He II and Ly$\alpha$; and (4) 3$\sigma$ upper limits of the rest-frame He II EW.

| Object | $FWHM_{int}(Ly\alpha)$ (km s$^{-1}$) | 3$\sigma$ $f_{He\,II}/f_{Ly\alpha}$ (Å) | 3$\sigma$ $EW_0$(He II) |
|---|---|---|---|
| (1) | (2) | (3) | (4) |
| COSMOS-08501 | 174 ± 38 | – | – |
| COSMOS-40792 | 118 ± 68 | $0.11^{+0.01}_{-0.02}$ | $91^{+38}_{-27}$ |
| COSMOS-41547 | 310 ± 78 | $0.10^{+0.01}_{-0.01}$ | $40^{+4}_{-3}$ |
| COSMOS-44993 | 238 ± 64 | $0.12^{+0.03}_{-0.02}$ | $41^{+5}_{-4}$ |
| SXDS1-10535 | 221 ± 30 | $0.08^{+0.01}_{-0.02}$ | $18^{+2}_{-2}$ |
| SXDS1-16564 | – | $0.02^{+0.01}_{-0.01}$ | $7^{+2}_{-2}$ |

values. Our conservative uncertainties in $\beta_{1800-2200}$ would include these systematic errors.

### 3.3 FWHM of Ly$\alpha$ lines

One of the advantages of our LAEs is that they have Ly$\alpha$ detections. We examine the FWHM of the Ly$\alpha$ line, FWHM(Ly$\alpha$). To derive FWHM(Ly$\alpha$) values, we apply a Monte Carlo technique exactly the same way as is adopted in Hashimoto et al. (2015). Briefly, we measure the 1$\sigma$ noise in the Ly$\alpha$ spectrum set by the continuum level at wavelengths longer than 1216 Å. Then we create $10^3$ fake spectra by perturbing the flux at each wavelength of the true spectrum by the measured 1$\sigma$ error. For each fake spectrum, the wavelength range which encompasses half the maximum flux is adopted as the FWHM. We adopt the median and standard deviation of the distribution of measurements as the median and error values, respectively. The measurements corrected for the instrumental resolutions, $FWHM_{int}(Ly\alpha)$, are listed in column 2 of Table 5. We do not obtain the $FWHM_{int}(Ly\alpha)$ of SXDS-C-16564 because its spectral resolution of the Ly$\alpha$ line, $R = 600$, is insufficient for a reliable measurement. Hereafter, we eliminate SXDS-C-16564 from the sample when we discuss the $FWHM_{int}(Ly\alpha)$ of our LAEs. $FWHM_{int}(Ly\alpha)$ values range from 118 to 310 km s$^{-1}$ with a mean value of 212 ± 32 km s$^{-1}$.

For comparisons, we also measure $FWHM_{int}(Ly\alpha)$ values of nine $z \sim 2$ LAEs with small $EW_0(Ly\alpha)$ values in the literature (Hashimoto et al. 2013, 2015; Nakajima et al. 2013; Shibuya et al. 2014b). Among the LAEs studied in these studies, we do not use COSMOS-30679 whose Ly$\alpha$ emission is contaminated by a cosmic ray (Hashimoto et al. 2013). Hereafter, we refer this sample as 'small $EW_0(Ly\alpha)$ LAEs'. The mean $EW_0(Ly\alpha)$ is 65 ± 10 Å, while the mean $FWHM_{int}(Ly\alpha)$ is calculated to be 389 ± 51 km s$^{-1}$. Table 6 summarizes the $EW_0(Ly\alpha)$ and $FWHM_{int}(Ly\alpha)$ values of the small $EW_0(Ly\alpha)$ LAEs.[1] In addition, Trainor et al. (2015) have also investigated Ly$\alpha$ profiles of LAEs at $z \sim 2.7$. For the composite spectrum of 32 LAEs which have both Ly$\alpha$ and nebular line detections, the typical $EW_0(Ly\alpha)$ value is 44 Å, while the mean $FWHM_{int}(Ly\alpha)$ value is 309 ± 22 km s$^{-1}$. Using a sample of the large $EW_0(Ly\alpha)$ LAEs, the small $EW_0(Ly\alpha)$ LAEs, and the LAEs and LBGs in Trainor et al. (2015), we plot $EW_0(Ly\alpha)$ as a function

[1] We note here that COSMOS-43982 has a signature of an AGN activity (Nakajima et al. 2013; Shibuya et al. 2014b; Hashimoto et al. 2015). We have confirmed that our discussion remains unchanged whether or not we include this object into the small $EW_0(Ly\alpha)$ LAEs.

**Table 6.** Properties of small $EW_0(Ly\alpha)$ LAEs. (1) Object ID; (2) rest-frame Ly$\alpha$ EWs; (3) FWHMs of the Ly$\alpha$ lines corrected for the instrumental resolutions; and (4) source of the information.

| Object | $EW_0(Ly\alpha)$ (Å) | $FWHM_{int}(Ly\alpha)$ (km s$^{-1}$) | Source[a] |
|---|---|---|---|
| (1) | (2) | (3) | (4) |
| CDFS-3865 | 64 ± 29 | 400 ± 15 | H13, N13, H15 |
| CDFS-6482 | 76 ± 52 | 350 ± 20 | H13, N13, H15 |
| COSMOS-13636 | 73 ± 5 | 292 ± 49 | H13, N13, H15 |
| COSMOS-43982[b] | 130 ± 12 | 368 ± 26 | H13, N13, H15 |
| COSMOS-08357 | 47 ± 8 | 460 ± 79 | S14, H15 |
| COSMOS-12805 | 34 ± 6 | 389 ± 23 | S14, H15 |
| COSMOS-13138 | 40 ± 10 | 748 ± 114 | S14, H15 |
| SXDS-10600 | 58 ± 3 | 217 ± 13 | S14, H15 |
| SXDS-10942 | 135 ± 10 | 274 ± 23 | S14, H15 |

*Notes.* [a]H13: Hashimoto et al. (2013); N13: Nakajima et al. (2013); S14: Shibuya et al. (2014b); H15: Hashimoto et al. (2015).
[b]AGN-like object.

of $FWHM_{int}(Ly\alpha)$ in Fig. 7. In this figure, the data points of Trainor et al. (2015) cover the small $EW_0(Ly\alpha)$ range complementary to our LAE results. We carry out the Spearman rank correlation test to evaluate the significance of a correlation. The rank correlation coefficient is $\rho = -0.72$, while the probability satisfying the null hypothesis is $P = 0.002$. The result indicates that $FWHM_{int}(Ly\alpha)$ anti-correlates with $EW_0(Ly\alpha)$. We also carry out the Spearman rank correlation test for objects with similar $M_{UV}$ values. For six LAEs satisfying $-20 \leqq M_{UV} \leqq -18$ (open circles in Fig. 7), we obtain $\rho = -0.94$ and $P = 0.016$. The result confirms that the anti-correlation is not due to the selection effect in $M_{UV}$. Although Tapken et al. (2007) have claimed a qualitatively similar anti-correlation between $EW_0(Ly\alpha)$ and $FWHM_{int}(Ly\alpha)$ for their small $EW_0(Ly\alpha)$ LAEs at a high-$z$ range of $z \sim 2.7$–4.5, no correlation test has been carried out. In our study, we have identified for the first time the anti-correlation based on a statistical test. Moreover, we have found the anti-correlation at the range of $EW_0(Ly\alpha) \gtrsim 200$ Å.

Several other studies have also studied $FWHM_{int}(Ly\alpha)$ values of LAEs at a high-$z$ range of $z \sim 3$–7. Tapken et al. (2007) have investigated $EW_0(Ly\alpha)$ and $FWHM_{int}(Ly\alpha)$ values of individual LAEs at $z \sim 2.7$–4.5. In this study, the mean $EW_0(Ly\alpha)$ is 47 ± 13 Å, while the mean $FWHM_{int}(Ly\alpha)$ is 472 ± 53 km s$^{-1}$. These values are consistent with those of the small $EW_0(Ly\alpha)$ LAEs (Table 6). At $z = 5.7$ and 6.6, Ouchi et al. (2010) have measured $FWHM_{int}(Ly\alpha)$ values of composite spectra of LAEs. The sample of Ouchi et al. (2010) does not include large $EW_0(Ly\alpha)$ LAEs. Nevertheless, the mean $FWHM_{int}(Ly\alpha)$ values are 265 ± 37 and 270 ± 16 km s$^{-1}$ for $z = 5.7$ and 6.6, respectively, smaller than those of the small $EW_0(Ly\alpha)$ LAEs (Table 6). This would be due to strong Ly$\alpha$ scattering in the IGM at $z \sim 6$–7 compared to that at $z \sim 2$: the IGM scattering significantly narrows the blue part of Ly$\alpha$ profile at $z \sim 6$–7 (Laursen, Sommer-Larsen & Razoumov 2011).

### 3.4 Upper limits on the flux ratio of He II/Ly$\alpha$ and $EW_0$(He II)

We derive 3$\sigma$ upper limits of the flux ratio, $f_{He\,II}/f_{Ly\alpha}$, where $f_{He\,II}$ and $f_{Ly\alpha}$ are the He II and Ly$\alpha$ fluxes, respectively. We do not derive the flux ratio for COSMOS-08501 whose FUV data have been obtained with MagE. This is because the flux calibration of echelle spectra is often inaccurate (Willmarth & Barnes 1994). Following the procedure in Kashikawa et al. (2012), we obtain the 3$\sigma$ upper limits of the He II fluxes. These He II fluxes are given

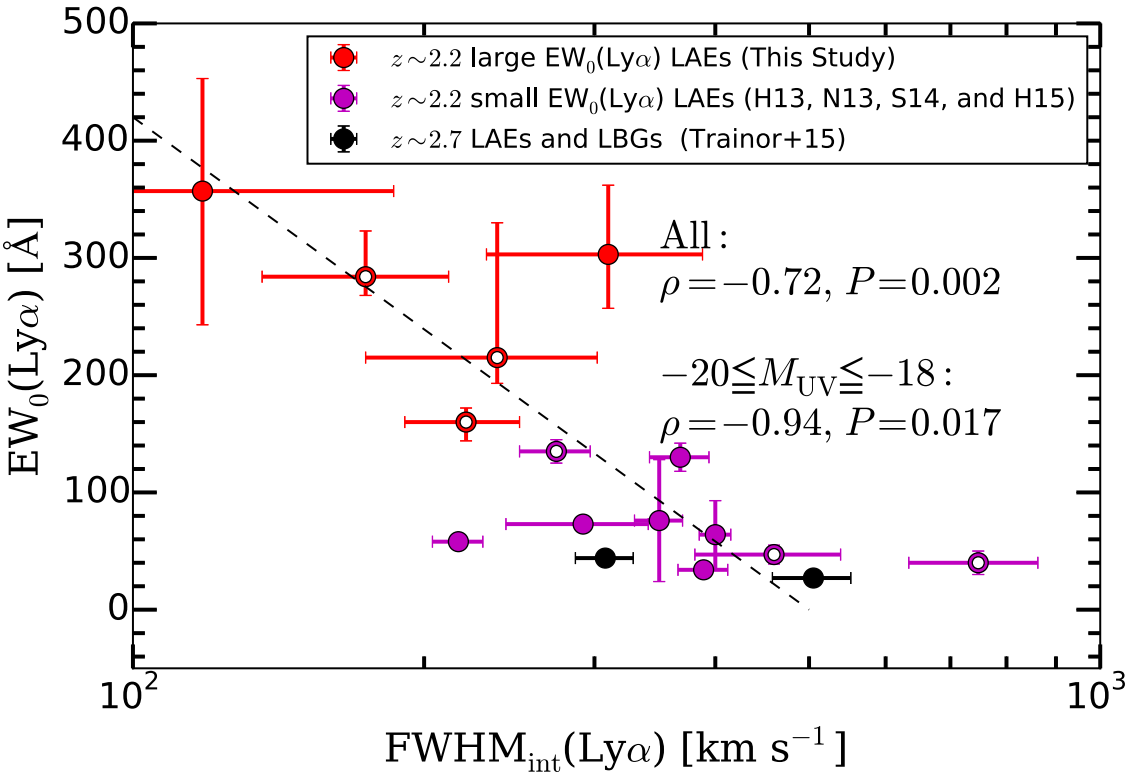


**Figure 7.** FWHM(Ly$\alpha$) corrected for the instrumental resolution, FWHM$_{\rm int}$(Ly$\alpha$), plotted against EW$_0$(Ly$\alpha$). Note that the $x$-axis is in the log-scale. The red circles are our large EW$_0$(Ly$\alpha$) LAEs at $z\sim2.2$, while the magenta circles indicate the small EW$_0$(Ly$\alpha$) LAEs at $z\sim2.2$ (Hashimoto et al. 2013, 2015; Nakajima et al. 2013; Shibuya et al. 2014b). The two black circles show the results for composite spectra of 32 LAEs and 65 LBGs at $z\sim2.7$ (Trainor et al. 2015). For the whole sample, the Spearman rank correlation coefficient for the relation is $\rho=-0.72$, while the probability satisfying the null hypothesis is $P=0.002$. The dashed line is the linear fit to the data points. The six open circles indicate the LAEs with similar $M_{\rm UV}$ values, $-20\leqq M_{\rm UV}\leqq-18$, respectively. For the six LAEs, the Spearman rank correlation test gives $\rho=-0.94$ and $P=0.017$.

from the wavelength ranges of 8.8 (4.8) Å for the IMACS (LRIS) spectra under the assumptions that the He II lines are not resolved. The derived 3$\sigma$ upper limits are $f_{\rm He\,II}/f_{\rm Ly\alpha}=0.11^{+0.01}_{-0.02}$ (COSMOS-40792), $0.10^{+0.01}_{-0.01}$ (COSMOS-41547), $0.12^{+0.03}_{-0.02}$ (COSMOS-44993), $0.08^{+0.01}_{-0.02}$ (SXDS-C-10535), and $0.02^{+0.01}_{-0.01}$ (SXDS-C-16564) (column 3 of Table 5). These 3$\sigma$ upper limits are stronger than the 2$\sigma$ upper limit of $f_{\rm He\,II}/f_{\rm Ly\alpha}=0.23$ derived for a strong LAE at $z=6.3$ (Nagao et al. 2005). Moreover, these 3$\sigma$ upper limits are comparable to the 3$\sigma$ upper limits of $f_{\rm He\,II}/f_{\rm Ly\alpha}\sim0.02$–$0.06$ obtained for LAEs at $z\sim3.1$–$3.7$ (Ouchi et al. 2008) and at $z=6.5$ (Kashikawa et al. 2012). Recently, Sobral et al. (2015) have reported the He II line detection from a strong LAE at $z=6.6$, CR7, at the significance level of 6$\sigma$. In this study, the rest-frame EW, EW$_0$(He II), is measured to be $\sim$80 Å [see also Bowler et al. (2016) who have obtained EW$_0$(He II) $=40\pm30$ Å with deep near-infrared photometric data]. The measured flux ratio of CR7 is $f_{\rm He\,II}/f_{\rm Ly\alpha}=0.23\pm0.10$.

We calculate the fraction of large EW$_0$(Ly$\alpha$) LAEs with He II detections among large EW$_0$(Ly$\alpha$) LAEs, combining our results with those in the literature. There are nine LAEs which satisfy EW$_0$(Ly$\alpha$) $\gtrsim$ 130 Å. These LAEs include five, one, one, and two objects from this study, Nagao et al. (2005), Kashikawa et al. (2012), and Sobral et al. (2015), respectively. We thus estimate the fraction to be $\sim$10 per cent (1/9).

We also examine 3$\sigma$ upper limits of the EW$_0$(He II). To do so, we derive the continuum flux at 1640 Å from photometric data with fitting results (Section 3.2). These estimates give us 3$\sigma$ limits of EW$_0$(He II) $\leqq 91^{+38}_{-27}$ Å (COSMOS-40792), $40^{+4}_{-3}$ Å (COSMOS-41547), $41^{+5}_{-4}$ Å (COSMOS-44993), $18^{+2}_{-2}$ Å (SXDS-C-10535), and $7^{+2}_{-2}$ Å (SXDS-C-16564) (column 4 of Table 5). We use the 3$\sigma$ upper limits of the EW$_0$(He II) to place constraints on the stellar ages and metallicities of our LAEs (Section 4.3).

### 3.5 Coarse estimates of the Ly$\alpha$ escape fraction

The Ly$\alpha$ escape fraction, $f_{\rm esc}^{\rm Ly\alpha}$, is defined as the ratio of the observed Ly$\alpha$ flux to the intrinsic Ly$\alpha$ flux produced in a galaxy. This quantity is mainly determined by a neutral hydrogen column density, $N_{\rm H\,I}$, or a dust content in the ISM. If the ISM has a low $N_{\rm H\,I}$ value or a low dust content, a high $f_{\rm esc}^{\rm Ly\alpha}$ value is expected because Ly$\alpha$ photons are less scattered and absorbed by dust grains (e.g. Atek et al. 2009; Hayes et al. 2011; Cassata et al. 2015).[2]

Many previous studies have estimated Ly$\alpha$ escape fractions on the assumptions of Case B, the Salpeter IMF, and the Calzetti dust extinction law. These assumptions would increase systematic uncertainties in the estimates of the Ly$\alpha$ escape fractions. Nevertheless, in order to compare Ly$\alpha$ escape fractions of our LAEs with those in the literature, we obtain Ly$\alpha$ escape fractions conventionally as

$$f_{\rm esc}^{\rm Ly\alpha}=\frac{L_{\rm obs}({\rm Ly\alpha})}{L_{\rm int}({\rm Ly\alpha})}, \quad (14)$$

[2] The outflowing ISM also facilitates the Ly$\alpha$ escape due to the reduced number of scattering (e.g. Kunth et al. 1998; Atek et al. 2008; Rivera-Thorsen et al. 2015).

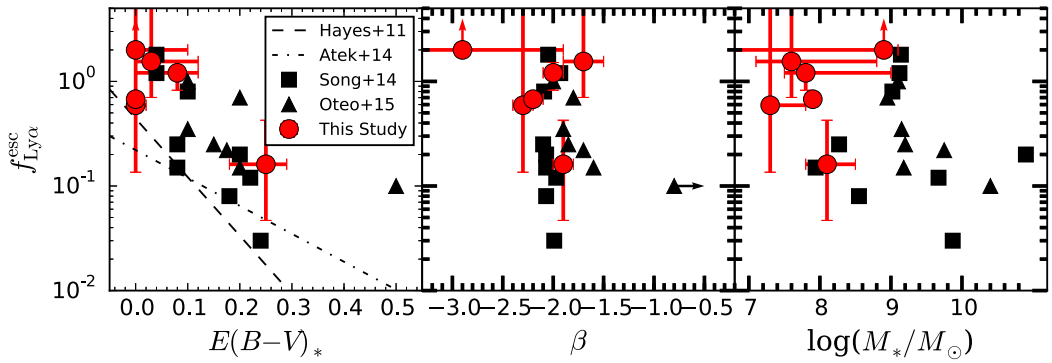


**Figure 8.** $f_{\rm esc}^{\rm Ly\alpha}$ plotted against $E(B-V)\star$, $\beta$, and $M\star$. The red circles denote our LAEs. The black squares are nine LAEs at $z\sim2$ with Ly$\alpha$ and H$\alpha$ detections (Song et al. 2014), whereas the black triangles show seven LAEs at $z\sim2$ with Ly$\alpha$ and H$\alpha$ (Oteo et al. 2015). In the left-hand panel, the dashed and dot–dashed lines indicate the relation between $f_{\rm esc}^{\rm Ly\alpha}$ and $E(B-V)\star$ for $z\sim0$–1 (Atek et al. 2014) and $z\sim2$–3 galaxies (Hayes et al. 2011), respectively. In the middle panel, we adopt $\beta_{1800-2200}$ for our LAEs.

where subscripts 'int' and 'obs' refer to intrinsic and observed quantities, respectively. We infer $L_{\rm int}$(Ly$\alpha$) from the SFRs in Table 3 using $L_{\rm int}$(Ly$\alpha$) [erg s$^{-1}$] $=1.1\times10^{42}$ SFR [M$_\odot$ yr$^{-1}$] (Kennicutt 1998) on the assumption of Case B. For COSMOS-08501 which has the H$\alpha$ detection, we quote the $f_{\rm esc}^{\rm Ly\alpha}$ value estimated from the extinction-corrected H$\alpha$ luminosities calculated by Nakajima et al. (2013). We have obtained $f_{\rm esc}^{\rm Ly\alpha}=1.21^{+0.31}_{-0.38}$ (COSMOS-08501), $5.33^{+2045}_{-0.91}$ (COSMOS-40792), $0.16^{+0.26}_{-0.11}$ (COSMOS-41547), $1.55^{+294}_{-0.85}$ (COSMOS-44993), $0.59^{+18}_{-0.45}$ (SXDS-C-10535), and $0.68^{+0.04}_{-0.05}$ (SXDS-C-16564). For the three objects which have relatively small errors, COSMOS-08501, COSMOS-41547, and SXDS-C-16564, the mean and median Ly$\alpha$ escape fractions are $f_{\rm esc}^{\rm Ly\alpha}=0.68\pm0.30$ and $0.68\pm0.30$, respectively. These values are much higher than the average Ly$\alpha$ escape fraction of $z\sim2$ galaxies, $f_{\rm esc}^{\rm Ly\alpha}\sim$2–5 per cent (Hayes et al. 2010; Steidel et al. 2011; Ciardullo et al. 2014; Oteo et al. 2015; Matthee et al. 2016), and even higher than the average value of $z\sim2$ LAEs, $f_{\rm esc}^{\rm Ly\alpha}\sim$10–37 per cent (Steidel et al. 2011; Nakajima et al. 2012; Kusakabe et al. 2015; Trainor et al. 2015; Erb et al. 2016; Sobral et al. 2016).

Fig. 8 plots $f_{\rm esc}^{\rm Ly\alpha}$ against $E(B-V)_*$, $\beta$, and $M\star$. We also plot the data points of $z\sim2$ LAEs studied by Song et al. (2014) and Oteo et al. (2015) with both Ly$\alpha$ and H$\alpha$ detections. In these studies, Ly$\alpha$ escape fractions have been estimated with H$\alpha$ luminosities. Although no individual measurements of UV continuum slopes are given in Song et al. (2014), we calculate $\beta_{1800-2200}$ values of the LAEs with equation (13) using the $V$-, $r$-, and $i$-band photometry listed in table 3 of Song et al. (2014). For the consistency, we adopt $\beta_{1800-2200}$ for our LAEs. Oteo et al. (2015) have shown that $f_{\rm esc}^{\rm Ly\alpha}$ anti-correlates with $E(B-V)_*$, $\beta$, and $M\star$. The result of Oteo et al. (2015) indicates that Ly$\alpha$ photons preferentially escape from low-mass and low dust content galaxies. With the median values of $E(B-V)_*=0.02^{+0.04}_{-0.02}$, $\beta_{1800-2200}=-2.2\pm0.2$, and $M\star=7.9^{+4.6}_{-2.9}\times10^7$ M$_\odot$, our LAEs can be regarded as the extreme cases in these trends.

## 4 DISCUSSION

### 4.1 Mode of star formation

There is a relatively tight relation between SFRs and stellar masses of galaxies called the star formation main sequence (SFMS; e.g. Daddi et al. 2007; Rodighiero et al. 2011; Speagle et al. 2014). Galaxies lying on the SFMS are thought to be in a long-term constant star formation mode, while those lying above the SFMS are forming stars in a rapid starburst mode (Rodighiero et al. 2011). We note here that the star formation mode is different from the SFH (see Section 3.1). As explained, star formation mode refers to the position of a galaxy in the relation between SFRs and stellar masses. In contrast, SFHs express the functional forms of SFRs, e.g. $e^{-t/\tau}$ for the exponentially declining SFH, where $t$ and $\tau$ indicate the age and the typical time-scale, respectively. The burst SFH indicates the declining SFH with $\tau<100$ Myr (e.g. Hathi et al. 2016). In the case of the constant SFH, the SFR is constant over time. With these in mind, we investigate the mode of star formation of our LAEs with SFRs and stellar masses in Section 3.1.

Fig. 9 plots SFRs against stellar masses for our LAEs. Fig. 9 also includes the data points of LAEs in the literature (Kusakabe et al. 2015; Taniguchi et al. 2015; Hagen et al. 2016), BzK galaxies (Rodighiero et al. 2011), and optical emission line galaxies (Hagen et al. 2016) at $z\sim$ 2–3. For COSMOS-08501, we also plot its SFR estimated from the extinction-corrected H$\alpha$ luminosities calculated by Nakajima et al. (2013). In Fig. 9, the median of the six large EW$_0$(Ly$\alpha$) LAEs is shown as the red star. The median data point indicates that our LAEs typically lie above the lower mass extrapolation of the $z\sim2$ SFMS (Daddi et al. 2007; Speagle et al. 2014). The specific SFRs (sSFR $\equiv$ SFR/$M\star$) of our LAEs are mostly in the range of sSFR $=$10–1000 Gyr$^{-1}$ with a median value of $\sim$100 Gyr$^{-1}$. The median sSFR of our LAEs is higher than those of LAEs and oELGs at $z\sim2$ in Hagen et al. (2016), $\sim$10 Gyr$^{-1}$.

Before interpreting the result, we note that stellar masses and SFRs in this study are derived from SED fitting on the assumption of the constant SFH. Thus, we need to check if our LAEs have high sSFRs on the assumption of other SFHs. Schaerer, de Barros & Sklias (2013) have examined how physical quantities depend on the choice of SFHs. This study includes exponentially declining, exponentially rising, and constant SFHs. As can be seen from figs 4 and 7 in Schaerer et al. (2013), stellar masses (SFRs) are the largest (smallest) for the constant SFH case among the various SFH cases. This means that the true sSFRs of our LAEs could be larger than what we have obtained. Therefore, our LAEs have high sSFRs regardless of the choice of SFHs.

A straightforward interpretation of the offset towards the high sSFR is that our large EW$_0$(Ly$\alpha$) LAEs are in the burst star formation mode. As discussed in detail by Hagen et al. (2016), the offset can also be due to (i) a possible change in the slope of the SFMS at the low-mass range, (ii) errors in the estimates of SFRs and stellar

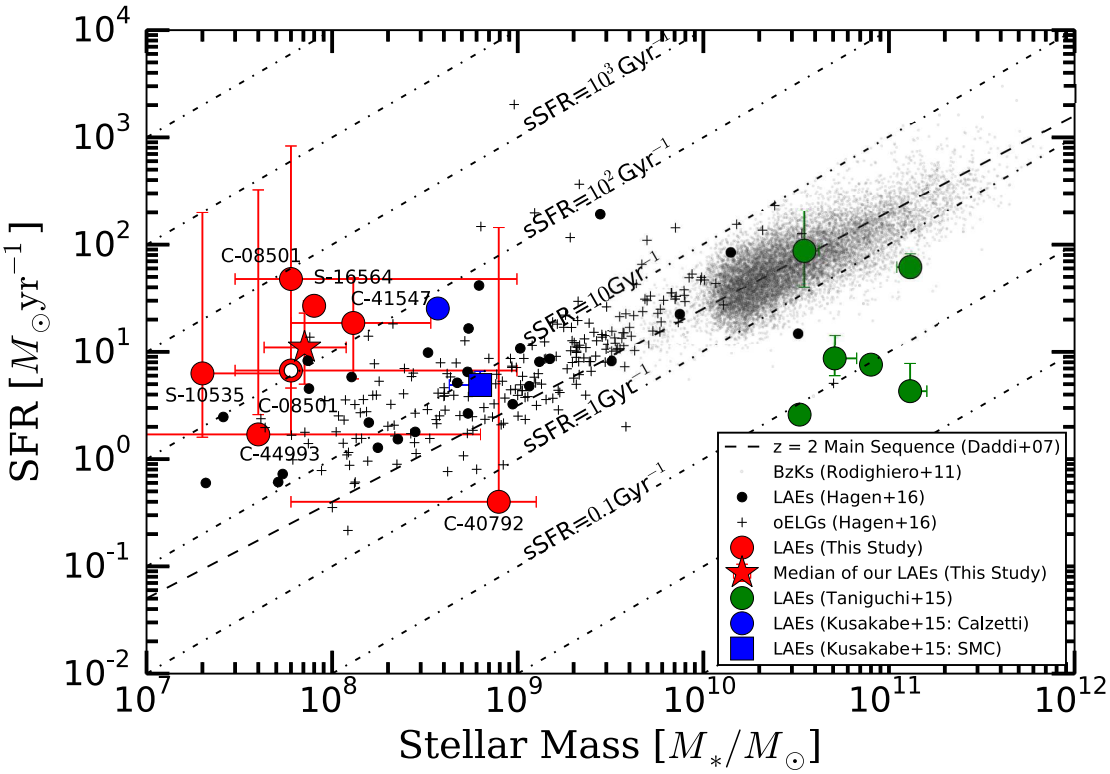


**Figure 9.** SFRs plotted against $M_\star$ for our large EW$_0$(Ly$\alpha$) LAEs and objects at $z \sim$ 2–3 in the literature, where dot–dashed lines represent specific SFRs (sSFR $\equiv$ SFR/$M_\star$). The red filled circles show our six large EW$_0$(Ly$\alpha$) LAEs with a median stellar mass of $M_* = 7.1^{+4.8}_{-2.8} \times 10^7$ M$_\odot$. The red open circle is COSMOS-08501 whose SFR is estimated from the extinction-corrected H$\alpha$ luminosities (Nakajima et al. 2013). The red star means the median of the six LAEs. The grey dots indicate $z \sim 2$ BzK galaxies (Rodighiero et al. 2011), while the dashed line shows the SFMS at $z = 2$ (Daddi et al. 2007). The black circles and crosses are luminous ($L$(Ly$\alpha$) $> 10^{43}$ erg s$^{-1}$) LAEs and optical emission line (e.g. [O II], H$\beta$, and [O III]) galaxies (oELGs) at $z \sim 2$ studied by Hagen et al. (2016), respectively. The green circles indicate $z \sim 3$ LAEs with large EW$_0$(Ly$\alpha$) values *and* evolved stellar populations (Taniguchi et al. 2015). The blue circle and square denote the results of the stacking of 214 $z \sim 2$ LAEs on the assumption of Calzetti's curve and the SMC attenuation curve, respectively (Kusakabe et al. 2015).

masses, or due to (iii) the selection bias against objects with high sSFRs at the low-mass range. As to the second point, Kusakabe et al. (2015) have shown that typical LAEs favour the Small Magellanic Cloud (SMC) attenuation curve (Pettini et al. 1998) rather than Calzetti's curve (Calzetti et al. 2000). Kusakabe et al. (2015) have demonstrated that SFRs are roughly 10 times overestimated if one uses Calzetti's curve (blue symbols in Fig. 9). However, we stress that our estimates of SFRs and stellar masses remain unchanged regardless of the extinction curve because our LAEs have small UV continuum slopes. Therefore, the second scenario is unlikely for our LAEs. As to the third point, Shimakawa et al. (2016) have investigated SFRs and stellar masses of LAEs with $M_\star > 10^8$ M$_\odot$ at $z \sim 2.5$. In contrast to our results and those in Hagen et al. (2016), LAEs in Shimakawa et al. (2016) follow the SFMS. Thus, it is possible that the high sSFRs of our LAEs are simply due to the selection bias. A large and uniform sample of galaxies with $M_\star = 10^{7-8}$ is needed for a definitive conclusion.

Recently, Taniguchi et al. (2015) have reported six rare LAEs at $z \sim 3$ which have large EW$_0$(Ly$\alpha$) values *and* evolved stellar populations. Their EW$_0$(Ly$\alpha$) values range from 107 to 306 Å with a mean value of 188 $\pm$ 30 Å. Taniguchi et al. (2015) have found that these LAEs lie *below* the SFMS, suggesting that these LAEs are ceasing star-forming activities. Based on the fact that our LAEs and those in Taniguchi et al. (2015) have similar EW$_0$(Ly$\alpha$) values, the EW$_0$(Ly$\alpha$) value is not necessarily a good indicator of the mode of star formation.

### 4.2 Interpretations of the small FWHM$_{\rm int}$(Ly$\alpha$) in large EW$_0$(Ly$\alpha$) LAEs

In Fig. 7, we have demonstrated that there is an anti-correlation between EW$_0$(Ly$\alpha$) and FWHM$_{\rm int}$(Ly$\alpha$). In this relation, our large EW$_0$(Ly$\alpha$) LAEs have small FWHM$_{\rm int}$(Ly$\alpha$) values. We give three interpretations of the small FWHM$_{\rm int}$(Ly$\alpha$) in our LAEs.[3]

First, assuming uniform expanding shell models, Verhamme et al. (2015) have theoretically shown that the small FWHM$_{\rm int}$(Ly$\alpha$) value is expected in the case of a low $N_{\rm H\,I}$ value in the ISM (see fig. 1 of Verhamme et al. 2015). If the physical picture of the theoretical study is true, the small FWHM$_{\rm int}$(Ly$\alpha$) of our large EW$_0$(Ly$\alpha$) LAEs suggest that our LAEs would have low $N_{\rm H\,I}$ values in the ISM.

Secondly, Gronke & Dijkstra (2016) have performed Ly$\alpha$ radiative transfer calculations of multiphase ISM models. The result shows that narrow Ly$\alpha$ profiles can be reproduced by two cases, one of which is on the condition that a galaxy has a low covering

[3] Zheng & Wallace (2014) have performed Ly$\alpha$ radiative transfer calculations with an anisotropic H I gas density. As can be seen from fig. 4 in Zheng & Wallace (2014), for a given $N_{\rm H\,I}$, the anisotropic H I gas density results in the anti-correlation between EW$_0$(Ly$\alpha$) and FWHM$_{\rm int}$(Ly$\alpha$). Thus, our results might simply indicate that the anisotropic H I gas density is at work in LAEs.

fraction of the neutral gas.[4] Thus, our large $EW_0(Ly\alpha)$ LAEs may have lower covering fractions of the neutral gas than small $EW_0(Ly\alpha)$ objects. Indeed, based on the analysis of the EW of low-ionization metal absorption lines, several studies have observationally shown that the neutral-gas covering fraction is low for galaxies with strong Ly$\alpha$ emission (e.g. Jones et al. 2013; Shibuya et al. 2014b; Trainor et al. 2015)

Finally, on the assumption that the $FWHM_{int}(Ly\alpha)$ value is determined by a dynamical mass to the first order, the small $FWHM_{int}(Ly\alpha)$ values of our large $EW_0(Ly\alpha)$ LAEs imply that our LAEs would have low dynamical masses compared to small $EW_0(Ly\alpha)$ objects. Although we admit that the $FWHM_{int}(Ly\alpha)$ value is dominantly determined by radiative transfer effects rather than dynamical masses, there is an observational result which may support this interpretation. Hashimoto et al. (2015) and Trainor et al. (2015) have found that $EW_0(Ly\alpha)$ anti-correlates with the FWHM value of nebular emission lines (e.g. H$\alpha$, [O III]), FWHM(neb). Since the FWHM(neb) value should correlate with the dynamical mass (e.g. Erb et al. 2006, 2014), the anti-correlation between $EW_0(Ly\alpha)$ and FWHM(neb) means that large $EW_0(Ly\alpha)$ LAEs have low dynamical masses. Among the large $EW_0(Ly\alpha)$ LAEs, COSMOS-8501 has the H$\alpha$ detection. However, only an upper limit of the FWHM of the H$\alpha$ line is derived because the line is not resolved (FWHM(neb) <200 km s$^{-1}$; Hashimoto et al. 2015). This prevents us from obtaining a definitive conclusion on which of the three interpretations are likely for our LAEs.

### 4.3 Constraints on stellar ages and metallicities

We place constraints on the stellar ages and metallicities of our LAEs by comparisons of our observational constrains of $\beta$, $EW_0(He\,II)$, and $EW_0(Ly\alpha)$ with the stellar evolution models of Schaerer (2003) and Raiter et al. (2010).

#### *4.3.1 Stellar evolutionary models*

Schaerer (2003) and the extended work of Raiter et al. (2010) have constructed stellar evolution models which cover various stellar metallicities ($Z = 0$–$1.0\ Z_\odot$), a variety of IMFs, and two SFHs of the instantaneous burst (burst SFH) and constant star formation (constant SFH). These studies have theoretically examined the evolutions of spectral properties including emission lines for the stellar ages from $10^4$ yr to 1 Gyr. From the theoretical computations, these studies have provided evolutions of $\beta$, $EW_0(He\,II)$, and $EW_0(Ly\alpha)$. To compute theoretical values of $EW_0(Ly\alpha)$ and $EW_0(He\,II)$, Schaerer (2003) and Raiter et al. (2010) have assumed Case B recombination. One of the advantages of the models of Schaerer (2003) and Raiter et al. (2010) is that the models have fine metallicity grids at an extremely low metallicity range. These fine metallicity grids are useful because large $EW_0(Ly\alpha)$ LAEs are thought to have extremely low metallicities. Among the results of Schaerer (2003) and Raiter et al. (2010), we use the predictions for six metallicities, $Z = 0$ (Pop III), $5 \times 10^{-6}$, $5 \times 10^{-4}$, 0.02, 0.2, and $1.0\ Z_\odot$. We adopt three power-law IMFs, (A) the Salpeter IMF at the mass range of 1–100 $M_\odot$, (B) the top-heavy Salpeter IMF at the mass range of 1–500 $M_\odot$, and (C) the Scalo IMF (Scalo 1986) at the mass range of 1–100 $M_\odot$. Table 7 summarizes the IMFs and their parameters.

[4] Another case is the low temperature and number density of the H I gas in the inter-clump medium of the multiphase ISM.

**Table 7.** Summary of IMF model parameters. (1) Model ID; (2) IMF; (3) line style in Fig. 10; (4) and (5) lower and upper mass cut-off values; and (6) IMF slope value.

| Model ID | IMF | Line type | $M_{low}$ ($M_\odot$) | $M_{up}$ ($M_\odot$) | $\alpha$ |
|---|---|---|---|---|---|
| (1) | (2) | (3) | (4) | (5) | (6) |
| A | Salpeter | Solid | 1 | 100 | 2.35 |
| B | Salpeter | Dotted | 100 | 500 | 2.35 |
| C | Scalo | Dashed | 1 | 100 | 2.75 |

Fig. 10 plots the evolutions of $\beta$, $EW_0(He\,II)$, and $EW_0(Ly\alpha)$. The top panels of Fig. 10 are the $\beta$ evolutions. $\beta$ values are sensitive to the stellar and nebular continuum. The $\beta$ evolution for extremely low metallicity cases ($Z = 0$–$5 \times 10^{-4}\ Z_\odot$) is significantly different from that for relatively high metallicity cases ($Z = 0.002$–$1.0\ Z_\odot$). We explain the burst SFH case. In the relatively high metallicity cases ($Z = 0.002$–$1.0\ Z_\odot$), the $\beta$ value monotonically increases as the stellar age increases. This is due to the fact that the dominant stellar continuum is red for old stellar ages. The value of $\beta \sim -2.7$ is expected at the very young stellar age of log(age yr$^{-1}$) ~6.0–7.0. In contrast, in the extremely low metallicity cases ($Z = 0$–$5 \times 10^{-4}\ Z_\odot$), the $\beta$ value behaves as a two-valued function. This is because the $\beta$ value is determined by both the stellar and nebular continuum at the extremely low metallicity cases. In these cases, the nebular continuum is very *red* for young stellar ages. Thus, at the very young stellar age of log(age yr$^{-1}$) ~6.0–6.5, the $\beta$ value is relatively large, $\beta \sim -2.3$, due to the balance between the red nebular continuum and the blue stellar continuum. The contribution of the red nebular continuum to the $\beta$ value becomes negligible at log(age yr$^{-1}$) $\gtrsim 7.0$ because of the rapid decrease of ionizing photons. Therefore, the $\beta$ value reaches down to $\beta \sim -3.0$ at log(age yr$^{-1}$) ~7.0–7.5, then monotonically increases. For the constant SFH, the evolution of $\beta$ is smaller than that of the burst SFH.

The second top panels of Fig. 10 show the $EW_0(He\,II)$ evolutions. The $EW_0(He\,II)$ value rapidly decreases as the metallicity increases: $EW_0(He\,II) > 5$ Å is expected only for $Z < 5 \times 10^{-6}\ Z_\odot$. In the case of the burst SFH, the time-scale for the He II line to be visible is short, log(age yr$^{-1}$) $\lesssim 7.0$. This time-scale reflects the lifetime of extremely massive hot stars. Again, the evolution of $EW_0(He\,II)$ is larger in the burst SFH than that of the constant SFH.

The bottom panels of Fig. 10 indicate the evolution of $EW_0(Ly\alpha)$. A high $EW_0(Ly\alpha)$ value is expected for a young stellar age and a low metallicity. In the case of the burst SFH, the time-scale for the Ly$\alpha$ line to be visible is log(age yr$^{-1}$) $\lesssim 7.5$. This reflects the lifetime of O-type stars. The maximum $EW_0(Ly\alpha)$ value can reach $EW_0(Ly\alpha)$ ~800–1500 Å for the Pop III metallicity.

#### *4.3.2 Comparisons of the observational constraints with the models*

Figs 11–13 compare the observational constraints of $\beta$, $EW_0(He\,II)$, and $EW_0(Ly\alpha)$ with the models. In these figures, grey shaded regions show the observed ranges of the three quantities. In the top panels, we show the intrinsic UV continuum slopes, $\beta_{1800-2200}$, for fair comparisons to the models (Section 3.2). In the second top panels, we present the upper limits of $EW_0(He\,II)$ (Section 3.4). The upper limits of $EW_0(He\,II)$ are obtained except for COSMOS-08501. As can be seen, these values are not strong enough to place constraints on the stellar age and metallicity. In the bottom panels, it should be noted that the models of Schaerer (2003) and Raiter

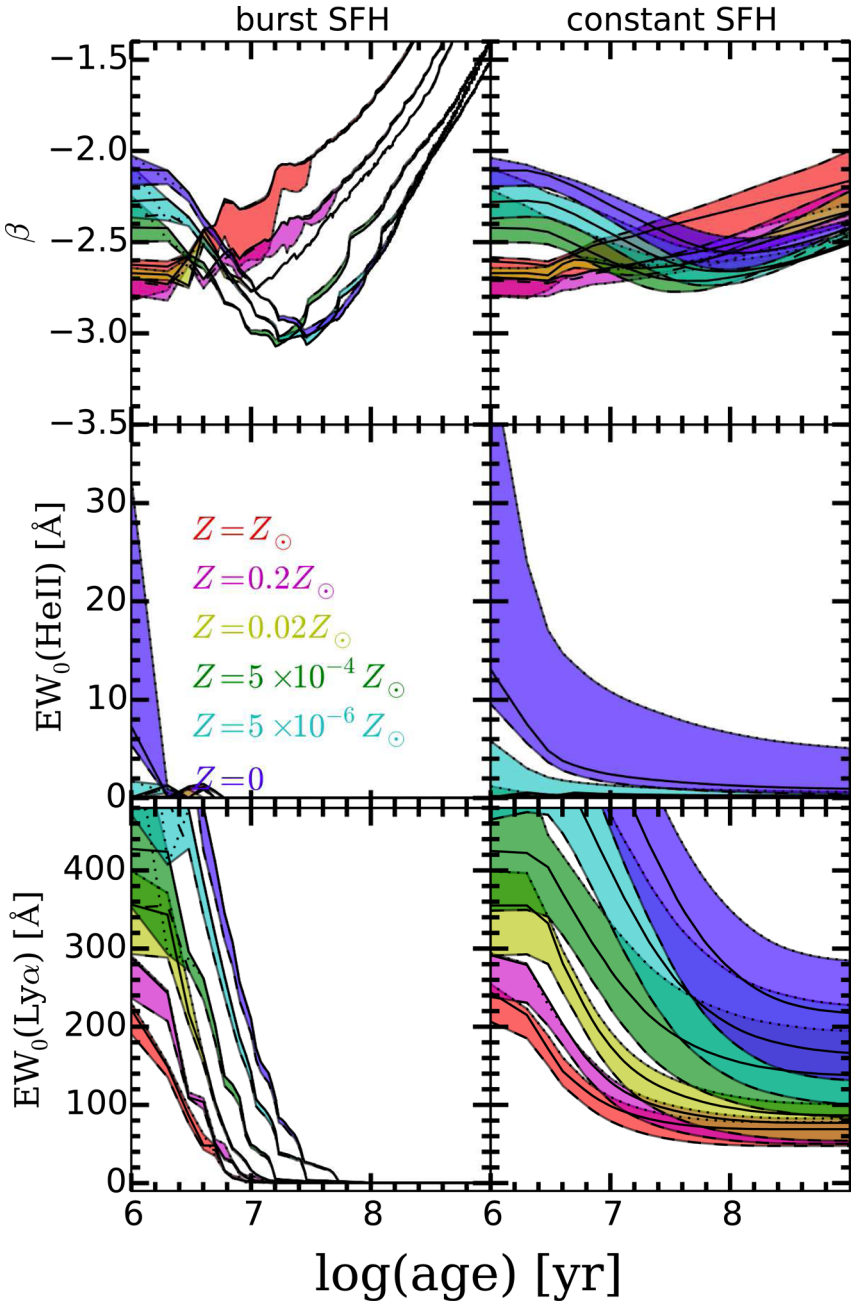


**Figure 10.** Theoretical evolutions of $\beta$, EW$_0$(He II), and EW$_0$(Ly$\alpha$) values. The left- and right-hand panels are the results for the burst SFH and constant SFH, respectively. For each panel, the solid, dotted, and dashed lines correspond to the IMFs of A, B, and C, respectively (Table 7). The blue, cyan, green, yellow, magenta, and red regions denote evolution ranges traced by the IMFs for metallicities of $Z = 0$, $5 \times 10^{-6}$, $5 \times 10^{-4}$, 0.02, 0.2, and 1.0 Z$_\odot$, respectively.

et al. (2010) do not take into account the effects of Ly$\alpha$ scattering/absorption in the ISM and IGM. Thus, in Figs 11–13, we plot the EW$_0$(Ly$\alpha$) values (Section 3.2) as the lower limits of the intrinsic EW$_0$(Ly$\alpha$) values for fair comparisons to the models.

In Figs 14 and 15, we plot the two ranges of the stellar ages and metallicities given by the $\beta$ and EW$_0$(Ly$\alpha$) values. The overlapped ranges of the two are adopted as the stellar ages and metallicities. Figs 14 and 15 clearly demonstrate that the combination of $\beta$ and EW$_0$(Ly$\alpha$) is powerful to constrain the stellar age and metallicity. Table 8 summarizes the permitted ranges of the stellar ages and metallicities of our LAEs. In Table 8, we find that our LAEs have generally low metallicities of $Z \lesssim 0.2\,Z_\odot$. Interestingly, it is implied that at least a half of our large EW$_0$(Ly$\alpha$) LAEs would have young stellar ages of $\lesssim$20 Myr and very low metallicities of $Z < 0.02$ Z$_\odot$ (possibly $Z \lesssim 5 \times 10^{-4}$ Z$_\odot$) regardless of the SFH. In Fig. 14, we cannot obtain the stellar age and metallicity which simultaneously satisfy the $\beta$ and EW$_0$(Ly$\alpha$) values of COSMOS-41547. This object has an exceptionally large correction factor for $\beta_{\rm obs.1800-2200}$, $-1.25^{+0.20}_{-0.35}$, compared to the median correction factor of $-0.1 \pm 0.2$ (Section 3.2). This is due to its large dust extinction value, $E(B-V)_* = 0.25^{+0.04}_{-0.07}$ (Table 3). Therefore, the stellar age and metallicity of COSMOS-41547 would be exceptionally affected by the systematic uncertainty discussed in Section 3.2. In Section 4.4, we consider other scenarios for the reason why the models have failed to constrain the stellar age and metallicity of COSMOS-41547.

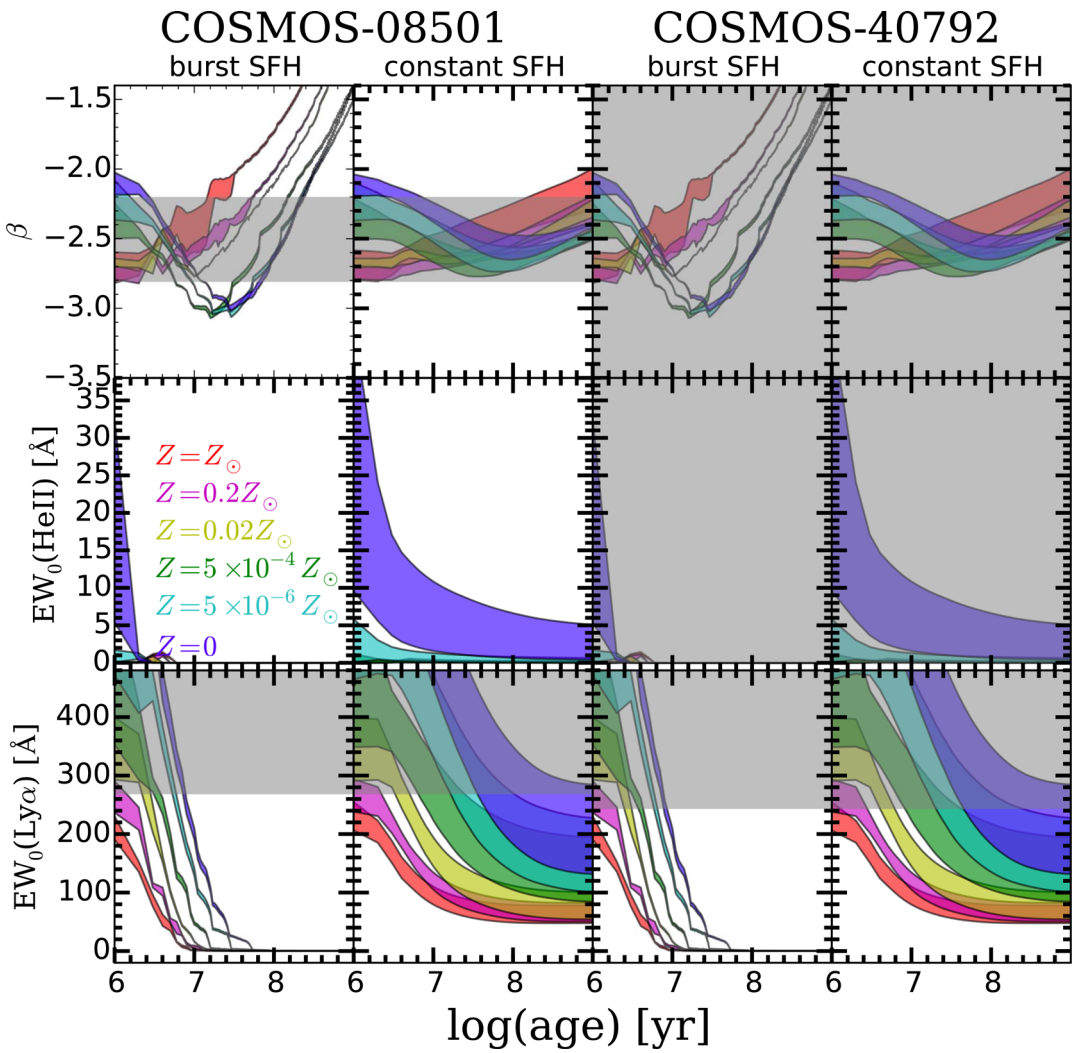


**Figure 11.** Comparisons of the observational constraints of $\beta$, $EW_0$(He II), and $EW_0$(Ly$\alpha$) with the models for COSMOS-08501 and COSMOS-40792. For each object, the left- and right-hand panels show the results for the burst SFH and constant SFH, respectively. The colour codes for the different metallicities are the same as those in Fig. 10. The horizontal grey shaded regions indicate the ranges of the observed quantities. In the top panels, we plot intrinsic $\beta$ values, $\beta_{1800-2200}$ (Section 3.2), which are corrected for dust attenuation effects on $\beta$. In the bottom panels, we plot $EW_0$(Ly$\alpha$) values (Table 4) as the lower limits of the intrinsic $EW_0$(Ly$\alpha$) values. This is because the models of Schaerer (2003) and Raiter et al. (2010) do not take into account the effects of Ly$\alpha$ scattering/absorption in the ISM and IGM.

Fig. 16 compares the two stellar ages, the one derived from SED fitting (Section 3.1) and the other obtained with the models of Schaerer (2003) and Raiter et al. (2010). The former and the latter stellar ages are referred to as $age_{BC03}$ and $age_{SR}$, respectively. The $age_{BC03}$ value is determined by past star formation activities. This is because the $age_{BC03}$ value is estimated from the photometric data which cover the rest-frame optical wavelength. In contrast, the $age_{SR}$ value represents the age of the most recent starburst activity. This is due to the fact that the $age_{SR}$ value is obtained from the rest-frame UV data alone. We find that the two stellar ages are consistent with each other within $1\sigma$ uncertainties regardless of the SFH. However, there is an exception, SXDS-C-16564 in the burst SFH case. In this case, the two stellar ages are consistent with each other within $2\sigma$ uncertainties. Among the two stellar ages, we adopt the $age_{SR}$ values as the stellar ages of our LAEs. This is because the $age_{SR}$ values are more realistic than the $age_{BC03}$ values in the sense that the $age_{SR}$ values are estimated with no assumption on the metallicity value.

#### 4.3.3 *Limitations of our discussion*

We have derived the stellar ages and metallicities of our LAEs with two assumptions. First, we have presumed the Case B recombination. As pointed out by Raiter et al. (2010) and Dijkstra (2014), significant departures from Case B are expected at the low-metallicity range of $Z \lesssim 0.03\ Z_{\odot}$ (see also Mas-Ribas, Dijkstra & Forero-Romero 2016). The departures can contribute to strong Ly$\alpha$ emission up to $EW_0$(Ly$\alpha$) $\sim$4000 Å because of (i) the increased importance of collisional excitation at the high gas temperature (ii) and the hard ionizing spectra emitted by metal-poor stars (Dijkstra 2014). The departures can also contribute to weak He II emission compared to Case B (Raiter et al. 2010). Thus, the constraints on the stellar age and metallicity may not be correct. Secondly, we have assumed a limited number of IMFs. Raiter et al. (2010) have argued that large uncertainties remain in the shape of the IMF of the metal-poor or metal-free stars. Therefore, the constraints on the stellar age and metallicity suffer from uncertainties due to the shape of the IMF.

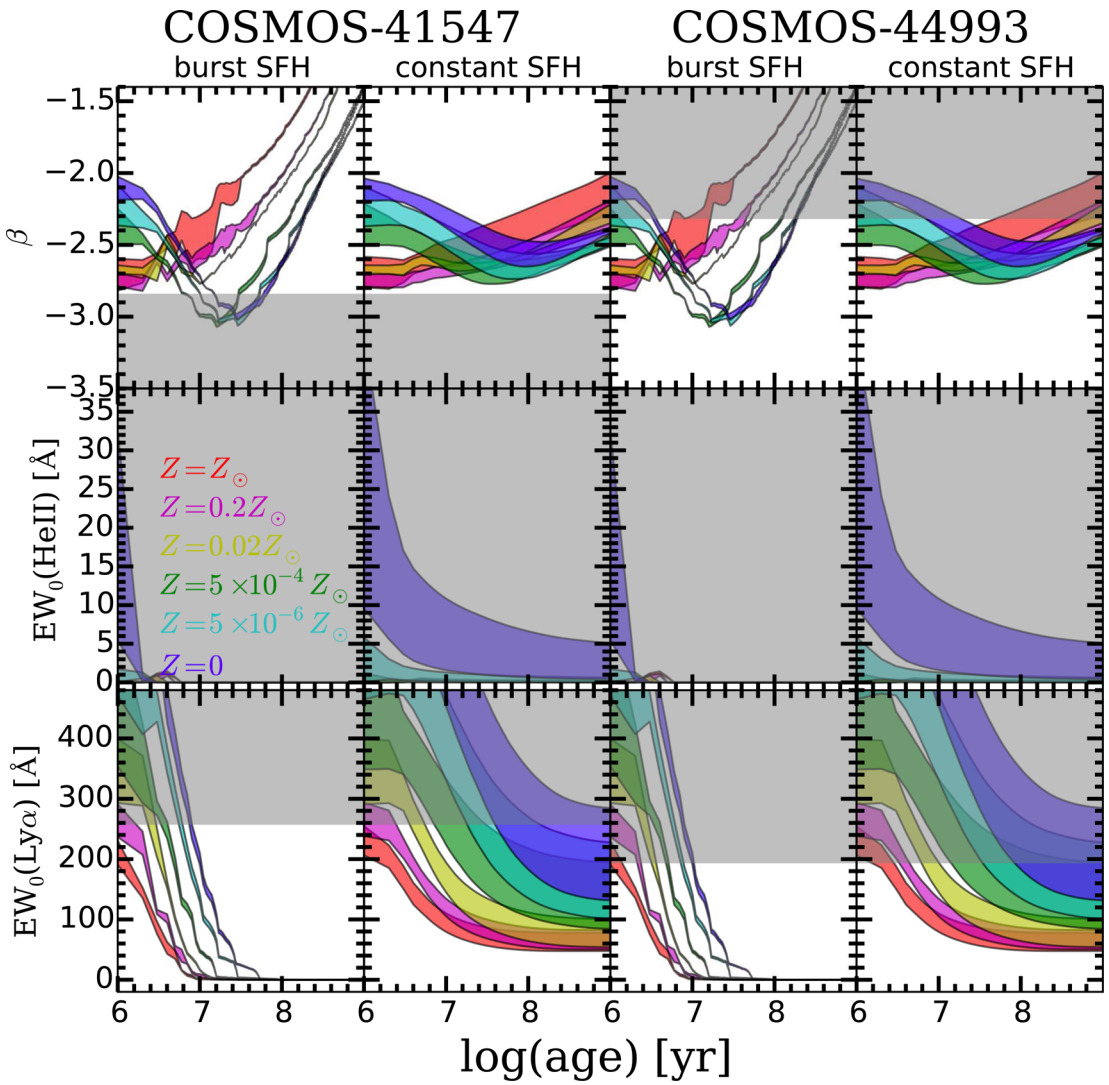


**Figure 12.** Same as Fig. 11 for COSMOS-41547 and COSMOS-44993.

### 4.4 Other scenarios of the large EW$_0$(Ly$\alpha$)

We have studied properties of our LAEs assuming that all Ly$\alpha$ photons are produced by star-forming activities. However, several other mechanisms can also generate Ly$\alpha$ photons. These include photoionization induced by (i) AGN activities (e.g. Malhotra & Rhoads 2002; Dawson et al. 2004) or (ii) external UV background sources such as QSOs (QSO fluorescence; e.g. Cantalupo et al. 2005; Cantalupo, Lilly & Haehnelt 2012). In addition, Ly$\alpha$ photons can be produced by collisional excitation due to (iii) strong outflows (shock heating; e.g. Taniguchi & Shioya 2000; Mori, Umemura & Ferrara 2004; Otí-Floranes et al. 2012) or (iv) inflows of gas into a galaxy (gravitational cooling; e.g. Haiman et al. 2000; Dijkstra & Loeb 2009; Rosdahl & Blaizot 2012). These mechanisms can enhance the Ly$\alpha$ production, leading to large EW$_0$(Ly$\alpha$) values. Moreover, (v) if a galaxy has a clumpy ISM, where dust grains are shielded by H I gas, EW$_0$(Ly$\alpha$) values can be apparently boosted. This is because Ly$\alpha$ photons are resonantly scattered on the surfaces of clouds without being absorbed by dust, while continuum photons are absorbed through dusty gas clouds (e.g. Neufeld 1991; Hansen & Oh 2006; Kobayashi, Totani & Nagashima 2010; Laursen, Duval & Östlin 2013; Gronke & Dijkstra 2014). We examine these five hypotheses.

*AGN activities.* AGN activities can enhance EW$_0$(Ly$\alpha$). However, we have confirmed that our LAEs do not host an AGN both on the individual and stacked bases (Section 2.4). The scenario is unlikely.

*QSO fluorescence.* According to the result of Cantalupo et al. (2005), QSOs can photoionize the outer layer of the ISM of nearby galaxies, enhancing EW$_0$(Ly$\alpha$) of the nearby galaxy. We examine this hypothesis in two ways. First, we have confirmed that there are no QSOs around any of our LAEs. Secondly, as discussed in Kashikawa et al. (2012), objects with fluorescent Ly$\alpha$ often do not have stellar-continuum counterparts. However, our LAEs clearly have stellar-continuum counterparts (Table 2). Therefore, we conclude that the QSO fluorescence hypothesis is unlikely.

*Shock heating.* Shock heating caused by strong outflows can produce Ly$\alpha$ photons (Taniguchi & Shioya 2000; Mori et al. 2004; Otí-Floranes et al. 2012). In this case, the Ly$\alpha$ morphology is expected to be spatially extended (Haiman et al. 2000; Taniguchi et al. 2015). However, our LAEs have spatially compact Ly$\alpha$ morphologies (Section 2.1). To obtain a definitive conclusion, it is useful to perform follow-up observations targeting [S II] and [N II] emission lines. This is because [S II] and [N II] emission lines are sensitive to the presence of shock heating (e.g. Newman et al. 2012). It is also interesting to perform follow-up observations targeting

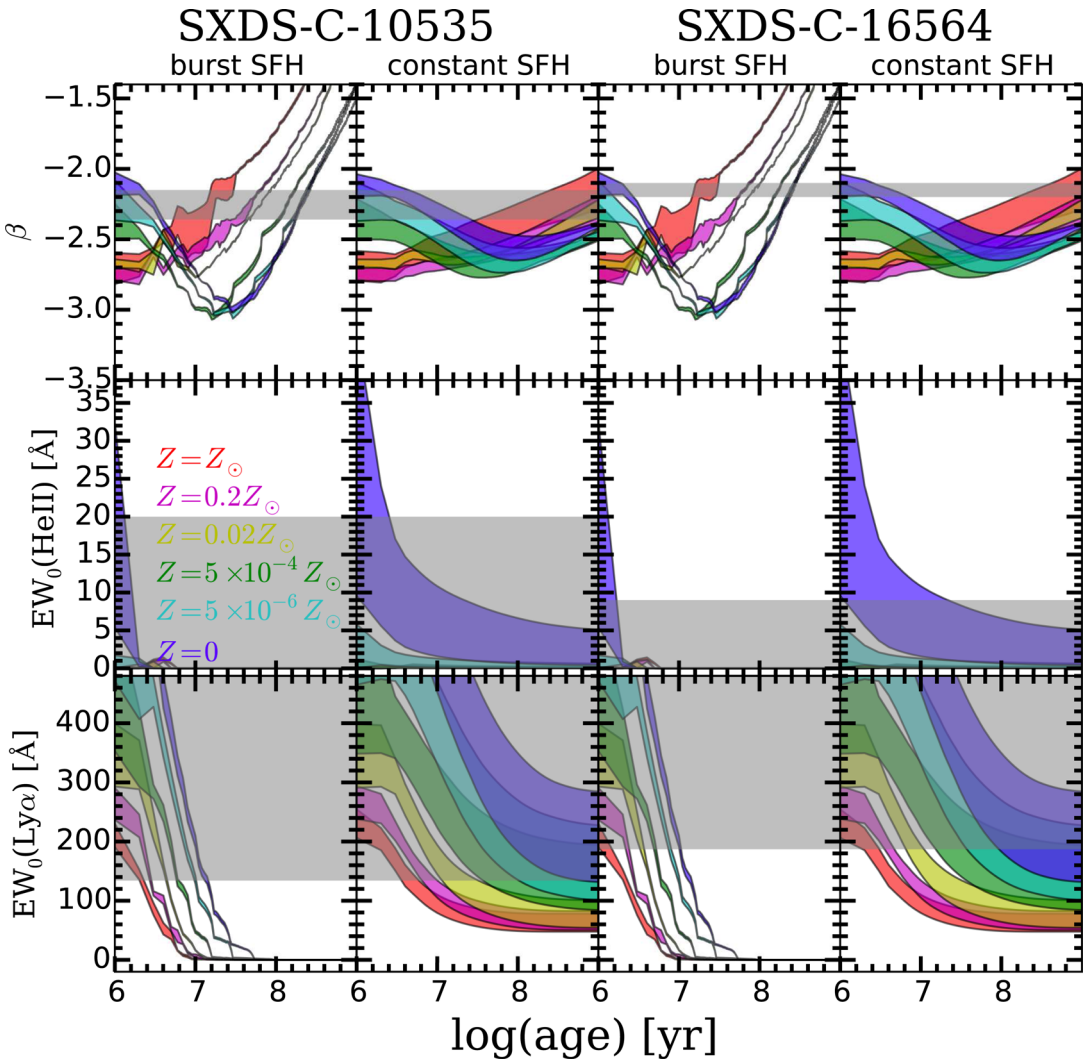


**Figure 13.** Same as Fig. 11 for SXDS-C-10535 and SXDS-C-16564.

metal absorption lines. With blueshifts of metal absorption lines with respect to the systemic redshifts, we can examine if outflow velocities are large enough to cause shock heating in our LAEs (e.g. Shapley et al. 2003; Shibuya et al. 2014b; Rivera-Thorsen et al. 2015).

*Gravitational cooling.* Ly$\alpha$ photons can also be generated by gravitational cooling. The gravitational binding energy of gas inflowing into a galaxy is converted into thermal energy, then released as Ly$\alpha$ emission. Ly$\alpha$ emission produced by gravitational cooling is predicted to be spatially extended (Rosdahl & Blaizot 2012). The compact Ly$\alpha$ morphologies of our LAEs do not favour the hypothesis. Deep H$\alpha$ data would help us to obtain a definitive conclusion. In the case of gravitational cooling, we expect a very high flux ratio of Ly$\alpha$ to H$\alpha$ lines, Ly$\alpha$/H$\alpha \sim 100$ (Dijkstra 2014). This high flux ratio can be distinguished from the ratio for the Case B recombination, Ly$\alpha$/H$\alpha = 8.7$.

*Clumpy ISM.* Finally, the gas distribution of LAEs may not be smooth. Duval et al. (2014) have theoretically investigated the condition of an ISM to boost EW$_0$(Ly$\alpha$) values. The EW$_0$(Ly$\alpha$) value can be boosted if a galaxy has an almost static (galactic outflows $<$200 km s$^{-1}$), clumpy, and very dusty ($E(B-V)_\star > 0.30$) ISM. The small median dust extinction value of our LAEs, $E(B-V)_* = 0.02^{+0.04}_{-0.02}$, would be at odds with the hypothesis.

In summary, no clear evidence of the five scenarios has been found in our LAEs.

In Section 4.3.2, we have shown that we cannot constrain the stellar age and metallicity of COSMOS-41547. One might think that the result is affected by e.g. a hidden AGN or collisional excitation. From Fig. 12, we have found that we can constrain the stellar age and metallicity of this object if more than 60 per cent of the observed Ly$\alpha$ flux is contributed from these additional mechanisms. If this is the case, we should see clear evidence of these effects. However, as we have shown, we do not see any clear evidence of these. Therefore, while the additional mechanisms could explain the failure of our method, the failure is most likely due to the systematic uncertainty as described in Section 4.3.2.

## 5 SUMMARY AND CONCLUSION

We have presented physical properties of spectroscopically confirmed LAEs with very large EW$_0$(Ly$\alpha$) values. We have identified six LAEs selected from $\sim$3000 LAEs at $z \sim 2$ with reliable measurements of EW$_0$(Ly$\alpha$) $\simeq$ 200–400 Å given by careful continuum determinations with our deep photometric and spectroscopic data. These LAEs do not have signatures of AGN. Our main results are as follows.

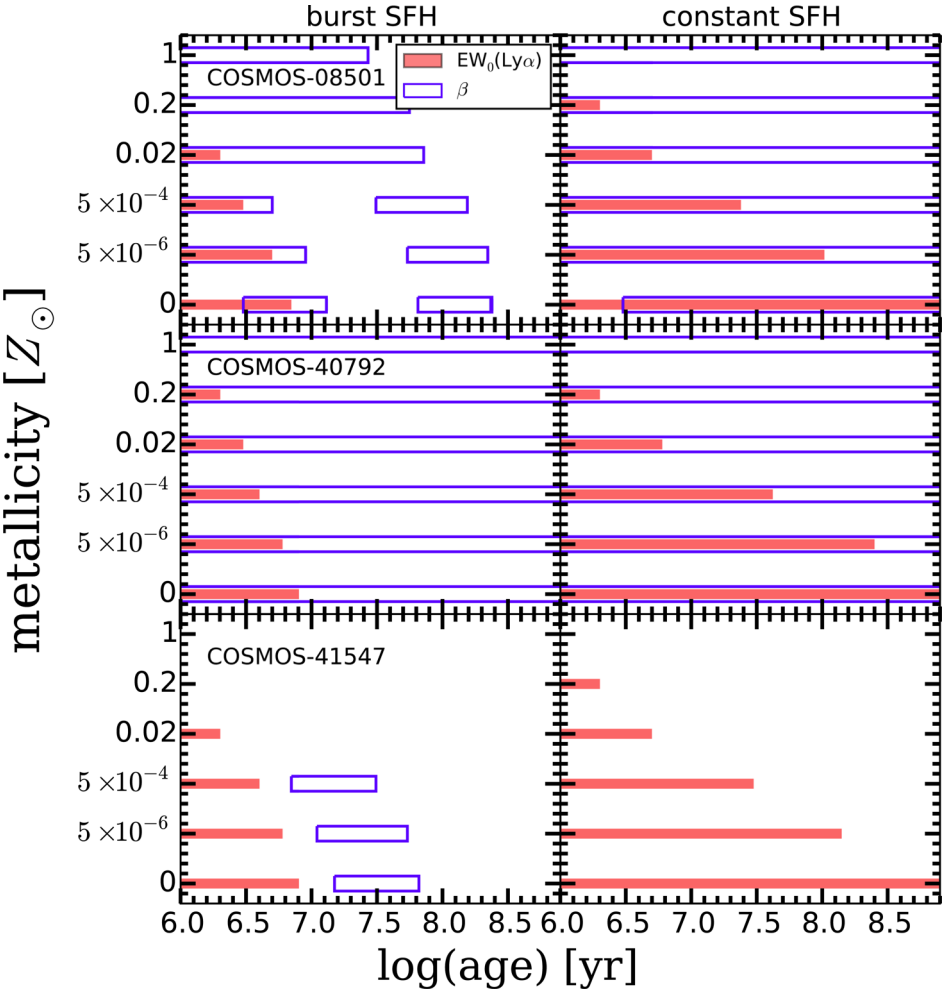


**Figure 14.** Left- and right-hand panels show permitted ranges of the stellar age and metallicity in the burst SFH and constant SFH, respectively, for COSMOS-08501, COSMOS-40792, and COSMOS-41547. The red filled squares and blue open squares denote the permitted ranges derived from the EW$_0$(Ly$\alpha$) and $\beta$ values, respectively. The overlapped regions of the red filled squares and blue open squares are the final constraints on the stellar mass and metallicity.

(i) We have performed SED fitting to derive physical quantities such as the stellar mass and dust extinction. Our LAEs have stellar masses of $M_\star = 10^{7-8}$ M$_\odot$ with a median value of $7.1^{+4.8}_{-2.8} \times 10^7$ M$_\odot$. The stellar masses of our LAEs are significantly smaller than those of small EW$_0$(Ly$\alpha$) LAEs at $z \sim 2$, $M_\star = 10^{8-10}$ M$_\odot$ (Nakajima et al. 2012; Oteo et al. 2015; Shimakawa et al. 2016). Our LAEs have stellar dust extinction values ranging from $E(B-V)_\star = 0.00$ to 0.25 with a median value of $0.02^{+0.04}_{-0.02}$. The median value is lower than that of small EW$_0$(Ly$\alpha$) LAEs at $z \sim 2$, $E(B-V)_\star = 0.2$–$0.3$ (Guaita et al. 2011; Nakajima et al. 2012; Oteo et al. 2015).

(ii) By modelling FUV photometric data with no a priori assumption on $\beta$ values, we find that our LAEs have EW$_0$(Ly$\alpha$) values ranging from EW$_0$(Ly$\alpha$) =160 to 357 Å, with a large mean value of 252 $\pm$ 30 Å. This confirms that LAEs with EW$_0$(Ly$\alpha$) $\gtrsim$ 200 Å exist. Our LAEs are characterized by the median values of $L$(Ly$\alpha$) $= 3.7 \times 10^{42}$ erg s$^{-1}$ and $M_{\rm UV} = -18.0$ as well as the small median UV continuum slope of $\beta = -2.5 \pm 0.2$.

(iii) Using stellar masses and SFRs derived from SED fitting, we have investigated our LAEs' star formation mode. With a high median sSFR ($\equiv$ SFR/$M_\star$) of $\sim$100 Gyr$^{-1}$, our LAEs typically lie above the lower mass extrapolation of the SFMS $z \sim 2$ defined by massive galaxies ($M_\star > 10^{10}$ M$_\odot$). An interpretation of the offset towards high sSFR is that our LAEs are in the burst star formation mode. However, the offset can also be due to (i) a different slope of the SFMS at the low stellar mass range or (ii) a selection effect of choosing galaxies with bright emission lines (i.e. high SFRs) at the low stellar mass range.

(iv) We have estimated the Ly$\alpha$ escape fraction, $f_{\rm esc}^{\rm Ly\alpha}$. For the three objects which have relatively small errors, the median value is calculated to be $f_{\rm esc}^{\rm Ly\alpha} = 0.68 \pm 0.30$. The high $f_{\rm esc}^{\rm Ly\alpha}$ value of our LAEs can be explained by the small dust content inferred from the small $E(B-V)_\star$ and $\beta$ values.

(v) Our large EW$_0$(Ly$\alpha$) LAEs have a small mean FWHM$_{\rm int}$(Ly$\alpha$) of 212 $\pm$ 32 km s$^{-1}$, significantly smaller than those of small EW$_0$(Ly$\alpha$) LAEs and LBGs at the similar redshift. Combined with small EW$_0$(Ly$\alpha$) LAEs and LBGs in the literature, we have statistically shown that there is an anti-correlation between EW$_0$(Ly$\alpha$) and FWHM$_{\rm int}$(Ly$\alpha$). The small FWHM$_{\rm int}$(Ly$\alpha$) values of our LAEs can be explained either by (i) low $N_{\rm H\,I}$ values in the ISM, (ii) low neutral-gas covering fractions of the ISM, or (iii) small dynamical masses.

(vi) We have placed constraints on the stellar ages and metallicities of our LAEs with the stellar evolution models of Schaerer (2003) and Raiter et al. (2010). Our observational constraints of the large EW$_0$(Ly$\alpha$), the small $\beta$, and EW$_0$(He II) imply

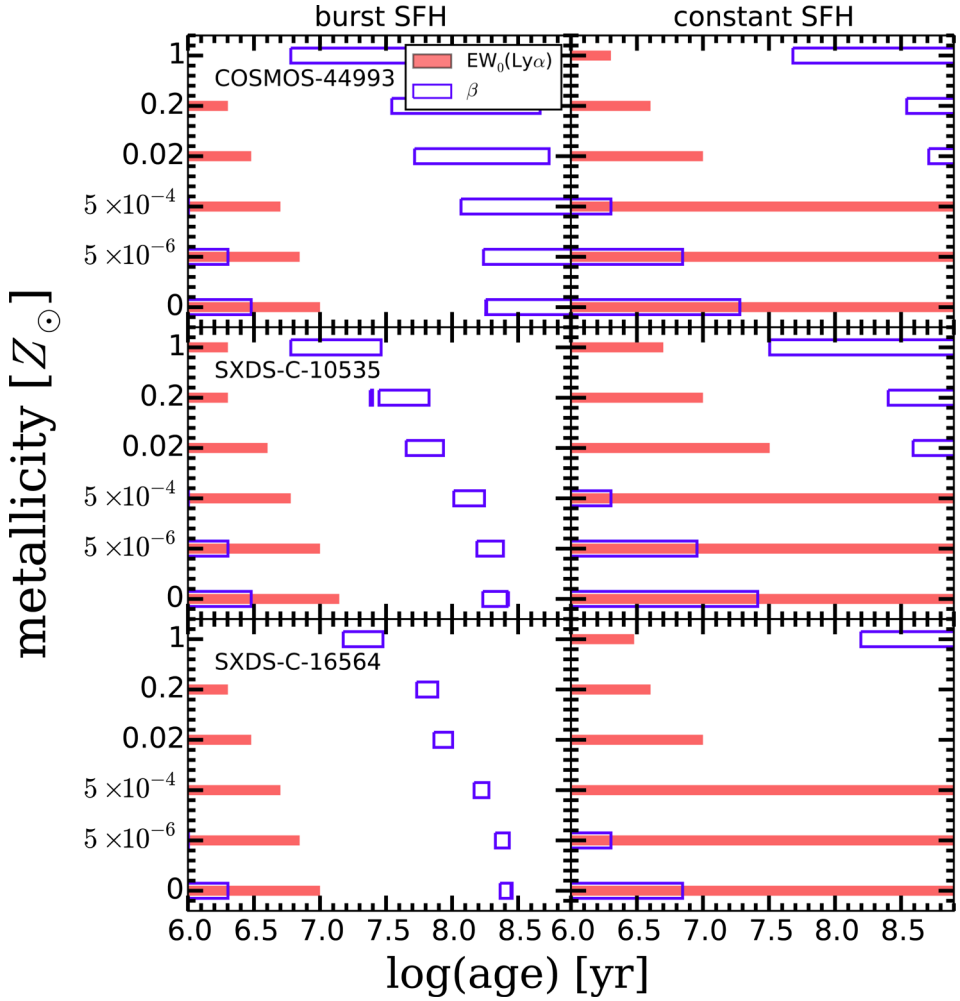


**Figure 15.** Same as Fig. 14 for COSMOS-44993, SXDS-C-10535, and SXDS-C-16564.

**Table 8.** Summary of stellar age and metallicity of our LAEs. (1) Object ID; (2) star formation history; and (3) permitted range of the stellar age for the each metallicity in the second row.

| Object ID (1) | SFH (2) | Stellar age (3) | | | | | |
|---|---|---|---|---|---|---|---|
| | | $Z/Z_\odot = 0$ | $5 \times 10^{-6}$ | $5 \times 10^{-4}$ | 0.02 | 0.2 | 1.0 |
| COSMOS-08501 | Burst | 3–8 Myr | <5 Myr | <3 Myr | <2 Myr | – | – |
| | Constant | 4–$10^3$ Myr | <100 Myr | <25 Myr | <5 Myr | <2 Myr | – |
| COSMOS-40792 | Burst | <8 Myr | <6.5 Myr | <5 Myr | <3.5 Myr | <2 Myr | – |
| | Constant | <$10^3$ Myr | <250 Myr | <40 Myr | <6.5 Myr | <2 Myr | – |
| COSMOS-41547 | Burst | – | – | – | – | – | – |
| | Constant | – | – | – | – | – | – |
| COSMOS-44993 | Burst | <3.5 Myr | <2 Myr | – | – | – | – |
| | Constant | <20 Myr | <8 Myr | <3 Myr | – | – | – |
| SXDS-C-10535 | Burst | <3.5 Myr | <2 Myr | – | – | – | – |
| | Constant | <25 Myr | <10 Myr | <2 Myr | – | – | – |
| SXDS-C-16564 | Burst | <2 Myr | – | – | – | – | – |
| | Constant | <8 Myr | <2 Myr | – | – | – | – |

that at least half of our large EW$_0$(Ly$\alpha$) LAEs would have young stellar ages of $\lesssim$20 Myr and very low metallicities of $Z < 0.02$ $Z_\odot$ regardless of the SFH.

(vii) We have investigated five other scenarios of the large EW$_0$(Ly$\alpha$) values of our LAEs: AGN activities, QSO fluorescence, shock heating, gravitational cooling, and the presence of the clumpy ISM. Our sample does not show any clear evidence of these hypotheses.

Among the results, the small $E(B-V)_\star$ and $\beta$ values are consistent with the high $f_{\rm esc}^{{\rm Ly}\alpha}$ values of our LAEs. The high $f_{\rm esc}^{{\rm Ly}\alpha}$ values are also consistent with the small FWHM(Ly$\alpha$) values

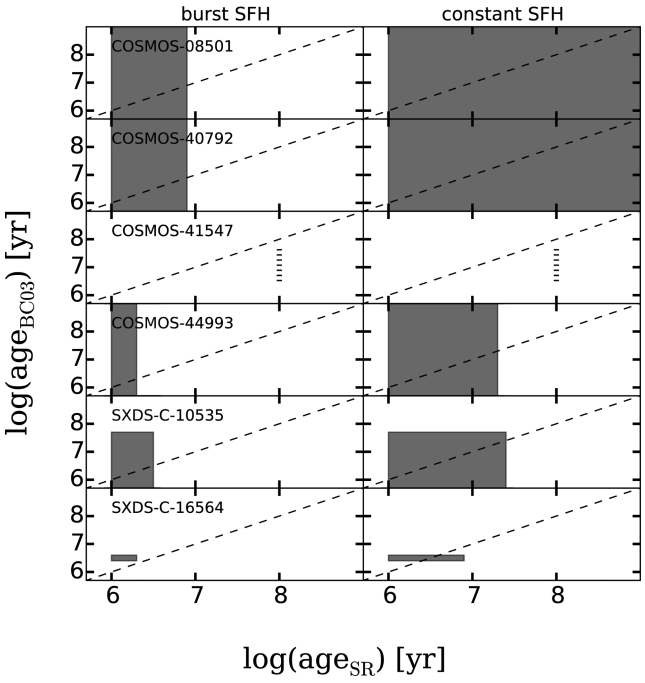


**Figure 16.** Comparisons of the two stellar ages of our LAEs, the one derived from SED fitting, age$_{BC03}$ (Section 3.1), and the other from the comparisons of observables to the models of Schaerer (2003) and Raiter et al. (2010), age$_{SR}$. For COSMOS-41547 whose age$_{SR}$ cannot be constrained (see the text), the vertical dashed line shows the range of age$_{SED}$. In the left-hand (right-hand) panels, the age$_{SR}$ values are obtained assuming the burst (constant) SFH. In each panel, the grey shaded region denotes the 1$\sigma$ ranges of the two stellar ages. The dashed line indicates the one-to-one relation.

indicative of the low H I column densities. We conclude that all of the low stellar masses, the young stellar ages, the low metallicities, and the high sSFR values are consistent with an idea that our large EW$_0$(Ly$\alpha$) LAEs represent the early stage of the galaxy formation and evolution with intense star-forming activities. The number of large EW$_0$(Ly$\alpha$) LAEs in this study is admittedly small. Hyper-Suprime Cam, a wide-field camera installed on Subaru, will be useful to increase the number of EW$_0$(Ly$\alpha$) LAEs at various redshifts.

## ACKNOWLEDGEMENTS

We thank an anonymous referee for valuable comments which have greatly improved the paper. We are grateful to Alex Hagen and Giulia Rodighiero for kindly providing us with their data plotted in Fig. 9. We also thank David Sobral, Tohru Nagao, Ken Mawatari, Ryota Kawamata, and Haruka Kusakabe for their helpful comments and suggestions. In addition, we acknowledge the organizers of Lyman Alpha as an Astrophysical Tool Workshop at Nordita Stockholm in 2013 September; this paper was enlightened by the talks and discussion which took place at that workshop. This work was supported by World Premier International Research Center Initiative (WPI Initiative), MEXT, Japan, and KAKENHI (23244022), (23244025), and (15H02064) Grant-in-Aid for Scientific Research (A) through Japan Society for the Promotion of Science (JSPS). TH acknowledges the JSPS Research Fellowship for Young Scientists. KN was supported by the JSPS Postdoctoral Fellowships for Research Abroad.

## REFERENCES

Adams J. J. et al., 2011, ApJS, 192, 5
Alavi A. et al., 2014, ApJ, 780, 143
Ando M., Ohta K., Iwata I., Akiyama M., Aoki K., Tamura N., 2006, ApJ, 645, L9
Atek H., Kunth D., Hayes M., Östlin G., Mas-Hesse J. M., 2008, A&A, 488, 491
Atek H., Kunth D., Schaerer D., Hayes M., Deharveng J. M., Östlin G., Mas-Hesse J. M., 2009, A&A, 506, L1
Atek H., Kunth D., Schaerer D., Mas-Hesse J. M., Hayes M., Östlin G., Kneib J.-P., 2014, A&A, 561, A89
Baldwin J. A., Phillips M. M., Terlevich R., 1981, PASP, 93, 5
Bertin E., Arnouts S., 1996, A&AS, 117, 393
Bouwens R. J. et al., 2009, ApJ, 705, 936
Bowler R. A. A., McLure R. J., Dunlop J. S., McLeod D. J., Stanway E. R., Eldridge J. J., Jarvis M. J., 2016, MNRAS, preprint (arXiv:1609.00727)
Brammer G. B. et al., 2012, ApJS, 200, 13
Bruzual G., Charlot S., 2003, MNRAS, 344, 1000
Calzetti D., Armus L., Bohlin R. C., Kinney A. L., Koornneef J., Storchi-Bergmann T., 2000, ApJ, 533, 682
Cantalupo S., Porciani C., Lilly S. J., Miniati F., 2005, ApJ, 628, 61
Cantalupo S., Lilly S. J., Haehnelt M. G., 2012, MNRAS, 425, 1992
Cassata P. et al., 2015, A&A, 573, A24
Charlot S., Fall S. M., 1993, ApJ, 415, 580
Ciardullo R. et al., 2012, ApJ, 744, 110
Ciardullo R. et al., 2014, ApJ, 796, 64
Cowie L. L., Hu E. M., 1998, AJ, 115, 1319
Daddi E. et al., 2007, ApJ, 670, 156
Dawson S. et al., 2004, ApJ, 617, 707
Dijkstra M., 2014, PASA, 31, e040
Dijkstra M., Loeb A., 2009, MNRAS, 396, 377
Duval F., Schaerer D., Östlin G., Laursen P., 2014, A&A, 562, A52
Elvis M. et al., 2009, ApJS, 184, 158
Erb D. K., Steidel C. C., Shapley A. E., Pettini M., Reddy N. A., Adelberger K. L., 2006, ApJ, 646, 107
Erb D. K. et al., 2014, ApJ, 795, 33
Erb D. K., Pettini M., Steidel C. C., Strom A. L., Rudie G. C., Trainor R. F., Shapley A. E., Reddy N. A., 2016, ApJ, 830, 52
Finkelstein S. L. et al., 2011, ApJ, 729, 140
Grogin N. A. et al., 2011, ApJS, 197, 35
Gronke M., Dijkstra M., 2014, MNRAS, 444, 1095
Gronke M., Dijkstra M., 2016, ApJ, 826, 14
Gronwall C. et al., 2007, ApJ, 667, 79
Guaita L. et al., 2011, ApJ, 733, 114
Hagen A. et al., 2016, ApJ, 817, 79
Haiman Z., Rees M. J., 2001, ApJ, 556, 87
Haiman Z., Spaans M., Quataert E., 2000, ApJ, 537, L5
Hansen M., Oh S. P., 2006, MNRAS, 367, 979
Hashimoto T., Ouchi M., Shimasaku K., Ono Y., Nakajima K., Rauch M., Lee J., Okamura S., 2013, ApJ, 765, 70
Hashimoto T. et al., 2015, ApJ, 812, 157
Hathi N. P. et al., 2013, ApJ, 765, 88
Hathi N. P. et al., 2016, A&A, 588, 26
Hayes M. et al., 2010, Nature, 464, 562
Hayes M., Schaerer D., Östlin G., Mas-Hesse J. M., Atek H., Kunth D., 2011, ApJ, 730, 8
Henry A., Scarlata C., Martin C. L., Erb D., 2015, ApJ, 809, 19
Jones T. A., Ellis R. S., Schenker M. A., Stark D. P., 2013, ApJ, 779, 52
Kashikawa N. et al., 2012, ApJ, 761, 85
Kennicutt R. C., Jr, 1998, ARA&A, 36, 189
Kobayashi M. A. R., Totani T., Nagashima M., 2010, ApJ, 708, 1119
Koekemoer A. M. et al., 2011, ApJS, 197, 36
Konno A., Ouchi M., Nakajima K., Duval F., Kusakabe H., Ono Y., Shimasaku K., 2016, ApJ, 823, 20
Kunth D., Mas-Hesse J. M., Terlevich E., Terlevich R., Lequeux J., Fall S. M., 1998, A&A, 334, 11

Kusakabe H., Shimasaku K., Nakajima K., Ouchi M., 2015, ApJ, 800, L29
Laursen P., Sommer-Larsen J., Razoumov A. O., 2011, ApJ, 728, 52
Laursen P., Duval F., Östlin G., 2013, ApJ, 766, 124
Madau P., 1995, ApJ, 441, 18
Malhotra S., Rhoads J. E., 2002, ApJ, 565, L71
Malhotra S., Rhoads J. E., 2004, ApJ, 617, L5
Mas-Ribas L., Dijkstra M., Forero-Romero J. E., 2016, ApJ, preprint (arXiv:1609.02150)
Matsuda Y. et al., 2004, AJ, 128, 569
Matthee J., Sobral D., Oteo I., Best P., Smail I., Röttgering H., Paulino-Afonso A., 2016, MNRAS, 458, 449
Mawatari K., Yamada T., Nakamura Y., Hayashino T., Matsuda Y., 2012, ApJ, 759, 133
Meurer G. R., Heckman T. M., Calzetti D., 1999, ApJ, 521, 64
Møller P., Warren S. J., 1998, MNRAS, 299, 661
Momose R. et al., 2014, MNRAS, 442, 110
Momose R. et al., 2016, MNRAS, 457, 2318
Mori M., Umemura M., Ferrara A., 2004, ApJ, 613, L97
Nagao T., Motohara K., Maiolino R., Marconi A., Taniguchi Y., Aoki K., Ajiki M., Shioya Y., 2005, ApJ, 631, L5
Nakajima K., Ouchi M., 2014, MNRAS, 442, 900
Nakajima K. et al., 2012, ApJ, 745, 12
Nakajima K., Ouchi M., Shimasaku K., Hashimoto T., Ono Y., Lee J. C., 2013, ApJ, 769, 3
Neufeld D. A., 1991, ApJ, 370, L85
Newman S. F. et al., 2012, ApJ, 761, 43
Nilsson K. K. et al., 2007, A&A, 471, 71
Nilsson K. K., Östlin G., Møller P., Möller-Nilsson O., Tapken C., Freudling W., Fynbo J. P. U., 2011, A&A, 529, A9
Oke J. B., Gunn J. E., 1983, ApJ, 266, 713
Ono Y. et al., 2010a, MNRAS, 402, 1580
Ono Y., Ouchi M., Shimasaku K., Dunlop J., Farrah D., McLure R., Okamura S., 2010b, ApJ, 724, 1524
Oteo I., Sobral D., Ivison R. J., Smail I., Best P. N., Cepa J., Pérez-García A. M., 2015, MNRAS, 452, 2018
Otí-Floranes H., Mas-Hesse J. M., Jiménez-Bailón E., Schaerer D., Hayes M., Östlin G., Atek H., Kunth D., 2012, A&A, 546, A65
Ouchi M. et al., 2003, ApJ, 582, 60
Ouchi M. et al., 2004, ApJ, 611, 660
Ouchi M. et al., 2008, ApJS, 176, 301
Ouchi M. et al., 2010, ApJ, 723, 869
Pettini M., Kellogg M., Steidel C. C., Dickinson M., Adelberger K. L., Giavalisco M., 1998, ApJ, 508, 539
Raiter A., Schaerer D., Fosbury R. A. E., 2010, A&A, 523, A64
Rhoads J. E., Malhotra S., Dey A., Stern D., Spinrad H., Jannuzi B. T., 2000, ApJ, 545, L85
Rivera-Thorsen T. E. et al., 2015, ApJ, 805, 14
Rodighiero G. et al., 2011, ApJ, 739, L40
Rosdahl J., Blaizot J., 2012, MNRAS, 423, 344
Salpeter E. E., 1955, ApJ, 121, 161
Scalo J. M., 1986, Fundam. Cosm. Phys., 11, 1
Schaerer D., 2002, A&A, 382, 28
Schaerer D., 2003, A&A, 397, 527
Schaerer D., de Barros S., 2009, A&A, 502, 423
Schaerer D., de Barros S., Sklias P., 2013, A&A, 549, 4
Schinnerer E. et al., 2010, ApJS, 188, 384
Shapley A. E., Steidel C. C., Pettini M., Adelberger K. L., 2003, ApJ, 588, 65
Shibuya T., Ouchi M., Nakajima K., Yuma S., Hashimoto T., Shimasaku K., Mori M., Umemura M., 2014a, ApJ, 785, 64
Shibuya T. et al., 2014b, ApJ, 788, 74
Shimakawa R. et al., 2016, preprint (arXiv:e-prints)
Shimasaku K. et al., 2006, PASJ, 58, 313
Skelton R. E. et al., 2014, ApJS, 214, 24
Sobral D., Matthee J., Darvish B., Schaerer D., Mobasher B., Röttgering H. J. A., Santos S., Hemmati S., 2015, ApJ, 808, 139
Sobral D. et al., 2016, MNRAS, preprint (arXiv:1609.05897)
Song M. et al., 2014, ApJ, 791, 3
Speagle J. S., Steinhardt C. L., Capak P. L., Silverman J. D., 2014, ApJS, 214, 15
Stark D. P., Ellis R. S., Chiu K., Ouchi M., Bunker A., 2010, MNRAS, 408, 1628
Stark D. P. et al., 2015, MNRAS, 450, 1846
Steidel C. C., Adelberger K. L., Shapley A. E., Pettini M., Dickinson M., Giavalisco M., 2000, ApJ, 532, 170
Steidel C. C., Erb D. K., Shapley A. E., Pettini M., Reddy N., Bogosavljević M., Rudie G. C., Rakic O., 2010, ApJ, 717, 289
Steidel C. C., Bogosavljević M., Shapley A. E., Kollmeier J. A., Reddy N. A., Erb D. K., Pettini M., 2011, ApJ, 736, 160
Taniguchi Y., Shioya Y., 2000, ApJ, 532, L13
Taniguchi Y. et al., 2015, ApJ, 809, L7
Tapken C., Appenzeller I., Noll S., Richling S., Heidt J., Meinköhn E., Mehlert D., 2007, A&A, 467, 63
Trainor R. F., Steidel C. C., Strom A. L., Rudie G. C., 2015, ApJ, 809, 89
Verhamme A., Orlitová I., Schaerer D., Hayes M., 2015, A&A, 578, A7
Villar-Martín M., Humphrey A., De Breuck C., Fosbury R., Binette L., Vernet J., 2007, MNRAS, 375, 1299
Wang J.-X., Malhotra S., Rhoads J. E., Zhang H.-T., Finkelstein S. L., 2009, ApJ, 706, 762
Willmarth D., Barnes J., 1994, Central Computer Services, NOAO
Zheng Z., Wallace J., 2014, ApJ, 794, 116
Zheng Z.-Y., Wang J.-X., Malhotra S., Rhoads J. E., Finkelstein S. L., Finkelstein K., 2014, MNRAS, 439, 1101

This paper has been typeset from a TEX/LATEX file prepared by the author.